JAMES | Journal of Advances in Modeling Earth Systems®

RESEARCH ARTICLE
10.1029/2025MS004992

Diurnal Variability Modulates Episodic Convection in Hothouse Climates Over Ocean and Swamp-Like Surface Conditions

Namrah Habib[1], **Guy Dagan**[1], **and Nathan Steiger**[1]

[1]Fredy and Nadine Herrmann Institute of Earth Sciences, Hebrew University, Jerusalem, Israel

Key Points:

- We study hothouse climates using radiative convective equilibrium simulations with a diurnal cycle over ocean and swamp-like conditions
- A transition from steady state to episodic precipitation occurs when accounting for diurnal variability at high surface temperatures
- The diurnal cycle modulates the episodic precipitation events with precipitation occurring primarily during the dawn or dusk hours

Correspondence to:
N. Habib,
namrah.habib@physics.ox.ac.uk

Citation:
Habib, N., Dagan, G., & Steiger, N. (2026). Diurnal variability modulates episodic convection in hothouse climates over ocean and swamp-like surface conditions. *Journal of Advances in Modeling Earth Systems*, *18*, e2025MS004992. https://doi.org/10.1029/2025MS004992

Received 31 JAN 2025
Accepted 29 JAN 2026

Abstract Hot and moist "hothouse" climates occurred in Earth's past and are expected in Earth's far future climate, driven by increasing solar luminosity. In hothouse climate regimes, precipitation transitions from a quasi-steady state, as in present-day tropical convection, to an "episodic deluge" or relaxation-oscillator (RO) regime where precipitation occurs in intense bursts separated by multi-day dry spells. Recent studies suggest that the transition to RO convection regimes is radiatively driven. However, the transition from steady state to RO convection has only been studied with radiative convective equilibrium (RCE) simulations with constant insolation, excluding the diurnal cycle. Precipitation and convection are strongly linked to the diurnal cycle in Earth's present climate over both land and ocean. We explore the impact of the diurnal cycle on the transition from steady state to RO convection using two sets of small-domain RCE simulations with ocean and swamp-like surface boundary conditions. Our RCE simulations with ocean boundary conditions show convection transitions to an episodic deluge regime at 322 K and the diurnal cycle modulates precipitation to occur during late-night or near dawn, when convective inhibition is the weakest. Our RCE simulations with swamp-like boundary conditions, which allow for mean surface temperature variations, show that as RO states emerge, the diurnal cycle modulates precipitation to primarily occur during the late-afternoon to about dusk; but as the mean SST increases, precipitation occurs during the late-night to dawn. These results show that the diurnal cycle strongly influences the timing of convection and precipitation patterns in extreme climates.

Plain Language Summary In hot and wet "hothouse" climate conditions, rainfall transitions from a pattern that fluctuates from about a mean of 3 mm day^{-1} to more intense outbursts that are separated by multi-day dry spells. Previous studies on hothouse climates did not consider the role of the diurnal cycle even though it strongly controls precipitation in Earth's current climate. This study uses radiative-convective equilibrium simulations to investigate the impact of rising temperatures on the transition to hothouse conditions, incorporating the diurnal cycle with both swamp-like and open ocean surface conditions. We find that episodic precipitation occurs at surface temperatures above 322 K even when accounting for the diurnal cycle. However, the diurnal cycle significantly influences the timing of convection and rainfall at high temperatures with precipitation primarily starting late at night or in the early morning.

1. Introduction

Observations and models of present-day convection in the Earth's tropics suggest that convection is nearly in statistical equilibrium with its environment. In this steady state, convection occurs frequently and precipitation is continuous, fluctuating around a mean rate of approximately 3 mm day^{-1}. However, in Earth's history, extremely hot and wet conditions, known as "hothouse" climates are thought to have existed (Charnay et al., 2017; Sleep, 2010). Further, as the Sun brightens due to stellar evolution, Earth will experience increasing solar luminosity and thus increasing temperatures leading to hothouse climate states before reaching a runaway greenhouse state (Popp et al., 2016; Seeley & Wordsworth, 2021; Wolf & Toon, 2015).

Previous studies investigating Earth's climate under hothouse climate conditions found that, at high temperatures, the water vapor infrared window becomes opaque. When the water vapor infrared window closes, lower-tropospheric radiative cooling observed under current climate conditions transitions to radiative warming (Popp et al., 2016; Seeley & Wordsworth, 2021; Wolf & Toon, 2015). Recently, Seeley and Wordsworth (2021) identified a fundamental shift in convection regimes at high surface temperatures, where convection transitions from a quasi-equilibrium (QE) steady state to an "episodic-deluge" or "relaxation-oscillator" (RO) regime, characterized by intense precipitation bursts separated by multi-day dry spells. Seeley and Wordsworth (2021)

attributed the shift in convection regime to lower-tropospheric radiative heating (LTRH), which creates an inhibition layer near the surface that decouples the lower and upper troposphere. During the dry spells, convective instability builds due to surface fluxes and upper tropospheric radiative cooling. Convection is triggered when rain evaporates at the top of the inhibition layer, producing latent cooling that erodes the inhibition layer and initiates an intense short-lived convective event that consumes the accumulated instability.

Subsequent studies of hothouse climates have further explored conditions under which RO convection regimes occur (e.g., Dagan et al., 2023; Dagan & Eytan, 2024; Song et al., 2023; Spaulding-Astudillo & Mitchell, 2024), as well as the mechanisms driving the RO convection behavior (e.g., Yang et al., 2024). Presently, there are two main hypotheses for the emergence of RO convection in hothouse climates. The first hypothesis is that the transition to a RO convective regime is radiatively driven (Song et al., 2023). While Seeley and Wordsworth (2021) proposed that RO convection is driven by LTRH, other studies (Dagan et al., 2023; Song et al., 2023; Spaulding-Astudillo & Mitchell, 2024) have shown that LTRH can facilitate the transition to RO states, but it is not a necessary condition for RO convection. Instead, Song et al. (2023) used convection-resolving models to analyze the effect of various radiative profiles with and without LTRH, and found that a strong contrast between the lower and upper tropospheric radiative heating rate triggers RO convection, even in the presence of lower-tropospheric radiative cooling.

The second hypothesis for the emergence of RO convection is the breakdown of quasi-equilibrium (QE) convection (Spaulding-Astudillo & Mitchell, 2024). In this framework, radiative convective equilibrium is treated as a heat engine, where the atmosphere acts as a closed system that converts heat, in the form of radiation, to work through some thermodynamic efficiency (Emanuel & Bister, 1996; Spaulding-Astudillo & Mitchell, 2024); this is specifically written as

$$-\eta F_a = |M| \times \mathrm{CAPE} \tag{1}$$

where η is the heat engine efficiency, F_a is the rate at which the system is heated through radiation, $|M|$ is the mass flux of air, and CAPE (convective available potential energy) is the work done by an air parcel lifted adiabatically through the atmosphere. In the QE convection regime, kinetic energy is generated and dissipated at equal rates creating steady state precipitation. The transition to RO convection occurs when the mass flux of air from the lower to the upper troposphere is insufficient to meet the energy demand of the heat engine. When $-\frac{\eta F_a}{|M|} >$ CAPE, QE convection breaks down. Without continuous convection, CAPE accumulates over time until $|M|$ is equal to the required mass flux of the heat engine at which point a convective event is triggered (Spaulding-Astudillo & Mitchell, 2024).

In the radiatively driven hypothesis (Song et al., 2023), the emergence of RO convection depends directly on radiative forcing. In contrast, in the heat engine hypothesis (Spaulding-Astudillo & Mitchell, 2024), radiation plays a key role in setting the energy budget, but is not explicitly modeled as the primary driver of RO emergence. In this work, we focus on how time-varying radiative conditions influence RO convection regimes.

Thus far, the transition to episodic precipitation has exclusively been studied in radiative-convective equilibrium (RCE) simulations that neglect diurnal variations of solar radiation (Seeley & Wordsworth, 2021; Song et al., 2023, etc.). RCE simulations with a diurnal cycle (e.g., Bechtold et al., 2004; Liu & Moncrieff, 1998; Nicholls, 2015; Sato et al., 2009) along with meteorological observations (e.g., Dai et al., 2007) have demonstrated the importance of diurnal precipitation patterns, with precipitation peaking in the afternoon or evening over land and during the night or early morning over open ocean.

Over the ocean, precipitation peaks during the night and early morning due to increased stability caused by shortwave heating during the day stabilizing the atmospheric column and suppressing moist convection (Liu & Moncrieff, 1998; Ruppert & Hohenegger, 2018; Sato et al., 2009). During the night, the absence of shortwave warming allows for radiative cooling to destabilize atmospheric stratification, thus leading to convective activity. However, other mechanisms such as sea surface temperature variations, and land-sea interactions have also been suggested to be important (Dingley et al., 2023; Haerter et al., 2020; Ruppert & Hohenegger, 2018; Sato et al., 2009).

Over land, precipitation peaks and primarily occurs in the afternoon or evening due to the diurnal cycle of surface heating (Bechtold et al., 2004; Haerter et al., 2020). Strong surface heating during the daytime creates an unstable

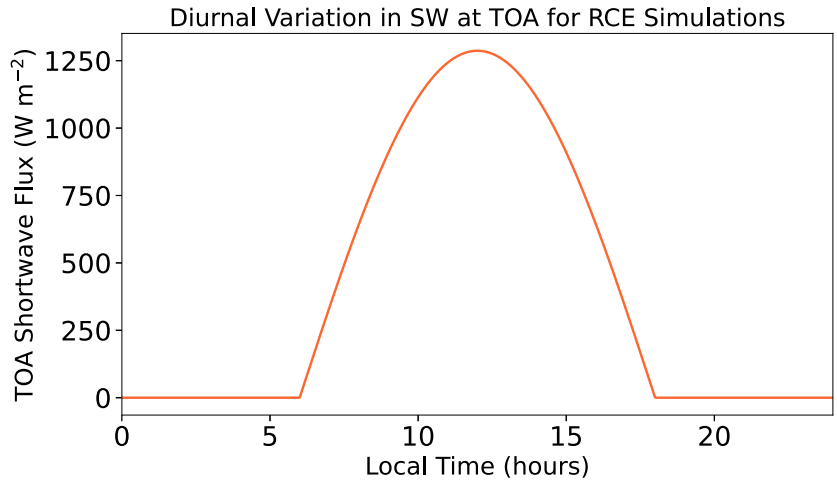

Figure 1. Diurnal variation in incoming shortwave (SW) flux at the top of the atmosphere (TOA), shown for one day, used in the RCE simulations. The SW diurnal forcing is applied to both the fixed SST and slab ocean simulations.

layer above the surface, which builds convective instability and triggers convection as surface temperatures reach their maximum.

Diurnal precipitation patterns are important in modulating convection in quasi-steady convection regimes and are completely unexplored for RO convection regimes. In this work, we examine how diurnal variability influences the transition from quasi-steady to RO convection as mean sea surface temperature (SST) increases. Accounting for the diurnal cycle on RO convection is expected to impact the LTRH, introducing diurnal variations in convective inhibition strength that could affect both the transition to and the behavior of RO convection.

To study the impact of diurnal variability on hothouse climates, we perform two sets of RCE simulations incorporating the diurnal cycle. The first RCE simulation set uses fixed SST ranging from 295 to 325 K with an open ocean surface boundary condition, allowing us to examine how the diurnal cycle affects precipitation and convection patterns as mean SST increases. The second set of RCE simulations explores the transition to an episodic convection regime using a thin slab ocean (which we refer to as "swamp-like" conditions) where the surface temperature is allowed to vary diurnally, with approximately the same magnitude as observed over land. Together, the two simulation sets with ocean and swamp-like surface boundary conditions, provide complementary views for studying the role of the diurnal cycle on RO convection and its precipitation patterns.

2. Methods

We perform radiative convective equilibrium (RCE) simulations using the System for Atmospheric Modeling (SAM) version 6.11.8 (M. F. Khairoutdinov & Randall, 2003). Sub-grid-scale turbulence is simulated using the Smagorinsky eddy diffusivity model while cloud microphysics are represented with SAM's one-moment cloud microphysics parameterization. All simulations are run with doubly periodic boundary conditions, and gravity waves are damped at the top of the domain. Radiative fluxes are computed once per 5 minutes using the Community Atmosphere Model (CAM) radiation scheme (Collins et al., 2006). Diurnal variability is modeled by using a time-varying insolation value set to zero from 6 p.m. to 6 a.m. and following a sinusoidal curve during the daylight hours based on the equatorial solar zenith angle calculated on day 0 of the year, as shown in Figure 1. The daily insolation peaks at approximately 1287 W m^{-2} at noon. The average insolation is approximately 413.8 W m^{-2} which is close to the current climate tropical-mean value. Trace gas concentrations, including ozone, follow Wing et al. (2018).

RCE simulations are initialized following the RCEMIP protocol (Wing et al., 2018). The vertical dimension is composed of 91 levels following the RCEMIP protocol up to 33 km, extending to 50 km with 1 km resolution to account for the increasing tropopause height at higher SSTs. The horizontal domain is 96×96 km^2 square domain with 1 km resolution. Simulations use a 5-s time step and the output resolution is 1 hr.

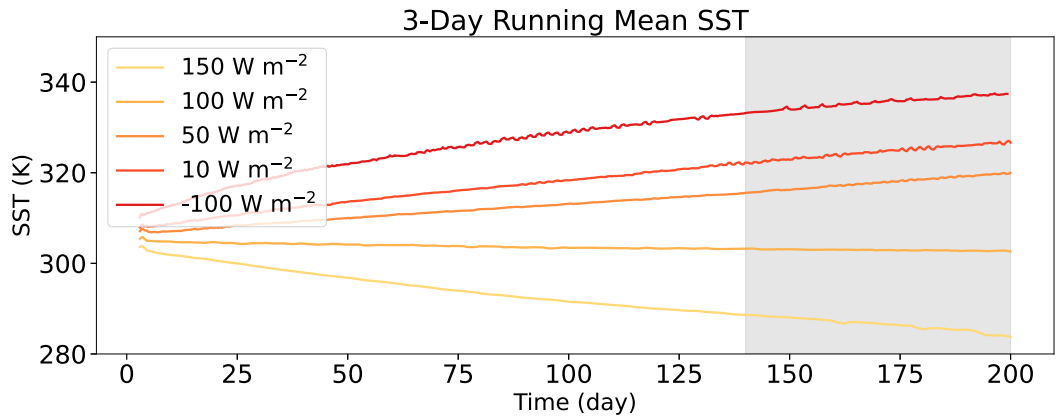

Figure 2. Three-day running mean SST for all 5 slab ocean cases over the course the entire 200 days simulation time frame. The simulations show that the mean SST gradually settles and slows its rate of change over the last 60 days, shown by the gray shaded region.

We performed two sets of RCE simulations: (a) homogeneous, fixed SST simulations with ocean boundary conditions, and (b) slab ocean simulations with diurnally varying surface temperatures, representing swamp-like boundary conditions. The fixed SST simulation setup is similar to Seeley and Wordsworth (2021) with the addition of the diurnal forcing in the incoming shortwave as shown by Figure 1. All fixed SST simulations are initialized with ocean surface boundary conditions. A total of 11 fixed SST simulations were performed. Six simulations were run with SSTs ranging from 295 to 320 K in 5 K increments and five simulations were initialized with SSTs ranging from 320 to 325 K in 1 K increments. Each fixed SST simulation is run for 100 days and the last 40 days are used in the results and analysis.

In the second simulation set, we performed RCE simulations with a thin slab ocean model, initialized with an SST of 300 K and a mixed layer depth of 0.2 m. Implementing a well-mixed slab ocean is a common approach (e.g., Dagan, 2022; Romps, 2020; Seeley & Wordsworth, 2021) to create simulations with time-varying SSTs to study the effects of any radiative forcings while allowing fast equilibration of the SST (Romps, 2020). Here, we use a shallow mixed layer depth to capture diurnal variations in surface temperature on the order of 10 K similar to surface temperature variations observed over land (Cronin et al., 2015; Haerter et al., 2020; Jensen et al., 2022; Ruppert & Hohenegger, 2018). Using a deep mixed layer depth dampens the diurnal SST variations, making diurnal variations practically negligible. At equilibrium, a deep mixed layer depth slab ocean simulation will behave similar to a fixed SST simulation. For instance, using a 0.2 m mixed layer depth creates diurnal surface temperature variations on the order of 10 K, whereas using a 50 m mixed layer depth will create diurnal surface temperature variations of about 0.2 K, similar to the fixed SST simulations. Further, simulations with deep 50 m mixed layer depth show the precipitation timeseries is nearly the same as in the fixed SST simulations (see the Appendix). Thus, to capture large diurnal variations in the surface temperature we use a shallow mixed layer depth. The shallow mixed layer depth slab ocean simulations still use an ocean boundary condition but allows for interactive SST changes due to the diurnal forcing, thus representing "swamp-like" boundary conditions.

We perform five slab ocean simulations with imposed fixed ocean heat fluxes of 10, 50, 100, 150 and -100 W m^{-2}. In slab ocean models, the ocean cannot redistribute heat horizontally, and a prescribed ocean heat sink is used to close the surface energy budget (Romps, 2020). In the real atmosphere, the energy imbalance is compensated by large-scale oceanic and atmospheric heat transports. Limited-area cloud-resolving models lack these processes, so an artificial ocean heat flux is used instead. In this work, the 100 W m^{-2} ocean heat flux corresponds to the top-of-atmosphere energy imbalance observed in the fixed SST run at 300 K. When a slab ocean flux of 100 W m^{-2} is applied, it approximately balances the net surface energy flux, leading to an SST that remains nearly constant over time (see Figure 2). Flux values greater than 100 W m^{-2} cause the mean SST to decrease with time as more heat is removed from the surface while lower flux values increase the mean SST with time (see Figure 2). Across the five slab ocean simulations, we vary the prescribed ocean heat flux to vary the mean SST while still allowing diurnal oscillations in the SST. Modifying only the slab ocean flux provides a simple and controlled way to change the

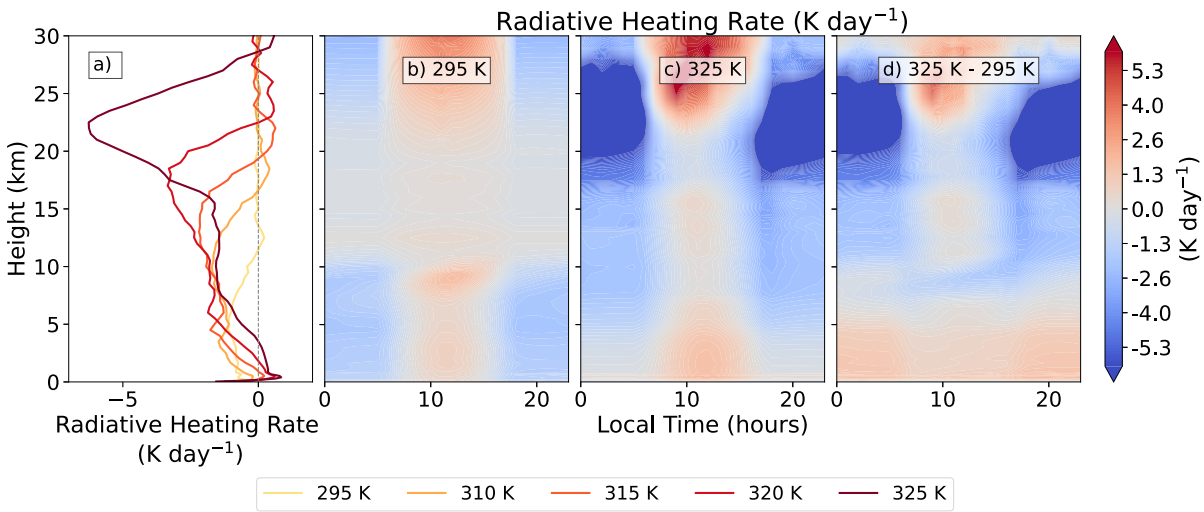

Figure 3. Daily averaged composite of radiative heating rate (K day^{-1}) as a function of height (km) and local time (hours) for (b) 295 K, (c) 325 K simulations, and (d) their difference. The radiative heating rate composites show stronger daytime heating and weaker nighttime cooling in the lower troposphere of the 325 K simulation relative to the 295 K simulation. Lower-tropospheric radiative heating (LTRH) is strongest during the day and weakest at the end of the night. Panel (a) shows the time and domain-averaged radiative heating rate (K day^{-1}) profiles for fixed SST simulations at 295 K (yellow), 310 K (orange), 315 K (red-orange), 320 K (red), and 325 K (maroon) averaged over the last 40 days. At lower SSTs, no LTRH is observed. However, as SST increases to 320 K and above, LTRH begins to develop.

mean SST without altering any other model parameters, thus making the simulations comparable and allowing us to understand how precipitation and the transition to RO convection is affected by diurnally varying SSTs.

All slab ocean simulations are initialized at an SST of 300 K and are run for 200 days, with the final 60 days used for analysis and results. These simulations are not intended to represent the equilibrium conditions, as the SST will continue to evolve even after 200 days but the mean SST slows in its rate of change over the course of the simulation, Figure 2. Simulations with an ocean heat flux of -100 W m^{-2} (representing heat added to the ocean) will eventually approach unstable conditions (Pierrehumbert, 2010) due to the increasing mean SSTs.

3. Results and Discussion

3.1. Fixed SST Simulations With Ocean Boundary Conditions

We begin our analysis by examining the radiative heating rate trends in the fixed SST simulations. Figure 3 shows the domain-averaged radiative heating rate profiles in panel (a) as well 24-hr composites of the average radiative heating rate in the last 40 days for the 295 and 325 K simulations in panel (b) and (c) respectively, and their difference in panel (d). Figure 3b and c shows the fixed SST simulations have nighttime radiative cooling throughout the atmosphere but daytime lower tropospheric radiative heating (LTRH). As the mean SST increases, the intensity of the daytime LTRH increases while the lower tropospheric nighttime cooling weakens (see Figure 3d). Generally, the net time-averaged radiative heating rate in Figure 3a shows that as the mean SST increases, lower tropospheric radiative cooling transitions to weak LTRH, while the radiative cooling in the upper atmosphere becomes stronger.

The baseline fixed SST simulation at 295 K represents the simulation most comparable to current climate conditions. Figure 4 presents the time series for (a) latent heating, (b) potential temperature within the inhibition layer, θ_{inhibit}, (c) moist static energy (MSE) near the surface, and (d) precipitation rate. θ_{inhibit} is taken as the average potential temperature between 390 and 1,660 m as this is where an inhibition layer forms in hotter simulations and where LTRH (if present) is observed. In Figure 4, yellow shaded regions show daytime hours where shortwave heating is greater than zero and gray shaded regions show nighttime hours. All variables in Figure 4 show diurnal variability. Precipitation (Figure 4d) peaks late at night or early in the morning, consistent with expectations for RCE simulations over open ocean (Liu & Moncrieff, 1998; Sato et al., 2009). During the day, shortwave heating (see Figure 3b) increases atmospheric stability, as seen through the increase in θ_{inhibit} and near surface MSE in Figures 4b and 4c, limiting the amount of convection and precipitation. At night, longwave

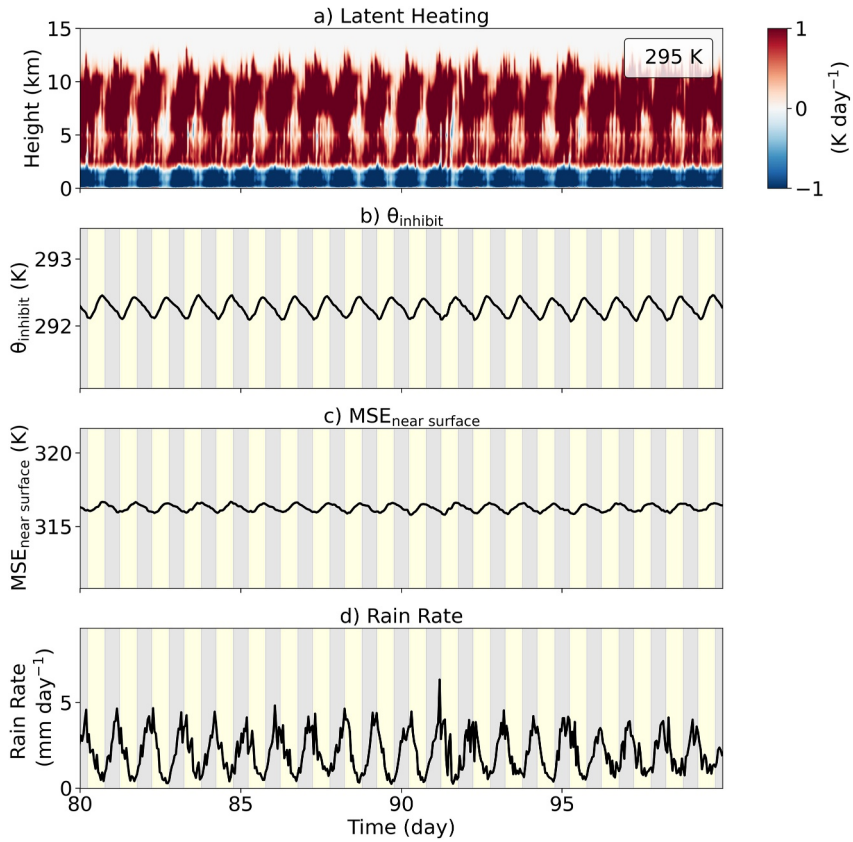

Figure 4. Time series of the final 20 days of the RCE simulation with fixed SST of 295 K showing domain-mean (a) latent heating (K day^{-1}), (b) potential temperature in the inhibition layer, $\theta_{inhibit}$(K), which is taken as the average potential temperature between 390 and 1,660 m, (c) moist static energy (MSE) near the surface (K), and (d) precipitation rate (mm day^{-1}). Gray shaded regions indicate nighttime hours, while yellow shaded regions represent daytime hours with nonzero insolation.

cooling destabilizes the atmosphere (corresponding to a decrease in $\theta_{inhibit}$ in Figure 4b), leading to stronger convection and increased precipitation. While convection is modulated by the diurnal cycle, it persists throughout the entire time period as seen by the continuous latent heat flux in Figure 4a, unlike RO convection regimes, where convection becomes fully suppressed with zero domain-mean precipitation at times.

Figure 5 compares the time series of the domain-mean precipitation rate for the fixed SST simulations ranging from 295 to 325 K in 5 K increments. As before, yellow shaded regions highlight daytime hours and gray shaded regions show nighttime hours. A black dashed line shows the time and domain mean precipitation rate in each panel. At SSTs between 295 and 320 K, precipitation oscillates due to the diurnal cycle, with precipitation primarily occurring in the nighttime. As SST increases from 300 to 320 K, the diurnal variation intensifies leading to stronger nighttime rain events. While during the day, convective stabilization gets stronger leading to subsequently reduced precipitation in the 300–315 K cases and complete suppression of convection and precipitation during the daytime in the 320 K case. Notably, comparing the precipitation rates across the panels in Figure 5 shows that while daytime heating reduces convection and precipitation as SST is increased from 295 to 320 K, the resulting daytime stabilization is not strong enough to fully suppress nighttime convection. For instance, the 320 K SST panel in Figure 5 shows that daytime convection is completely suppressed, as indicated by the absence of precipitation. However, precipitation still occurs during the latter half of the night suggesting that the inhibition layer breaks down during the nighttime. A clear shift to RO convection is observed at 325 K where precipitation occurs in short intense bursts, separated by multi-day dry spells.

To examine the transition from a quasi-steady state to RO convection, Figure 6 shows the precipitation rate time series over the final 20 days for fixed SST simulations from 320 to 325 K in 1 K increments. At 320 and 321 K, precipitation occurs once daily, typically from the late night to early morning hours. Daytime shortwave heating

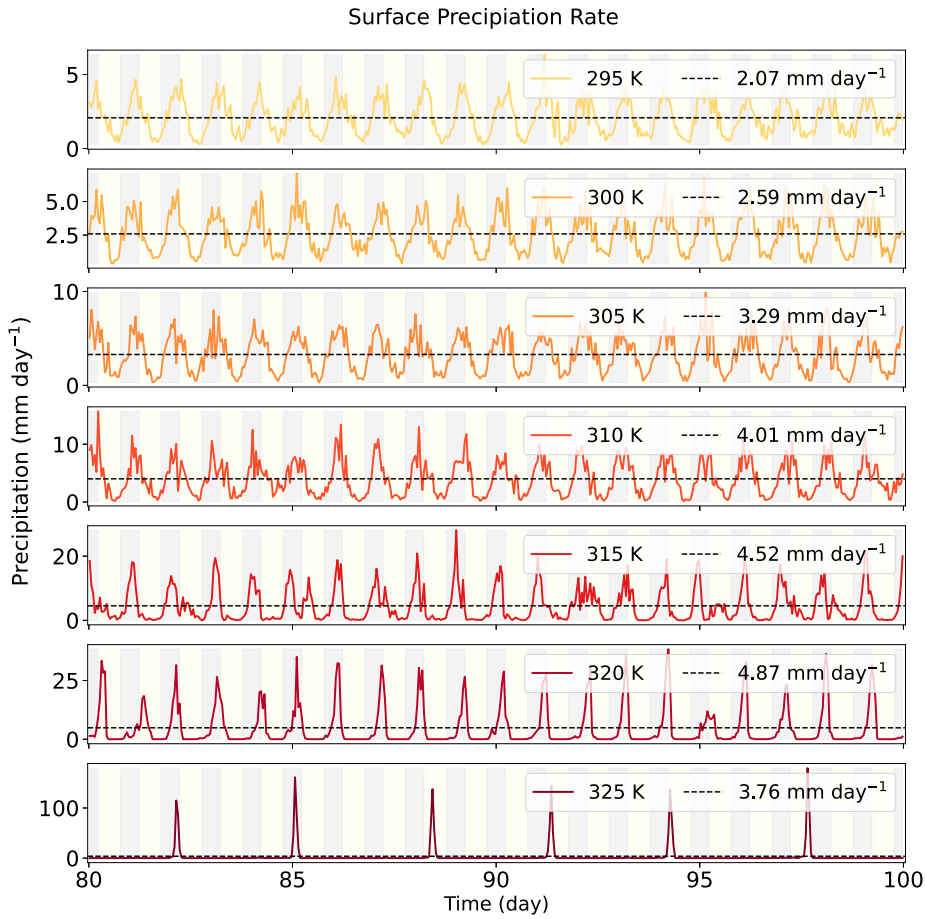

Figure 5. The domain-mean precipitation rate for RCE simulations with fixed SST from 295 to 325 K in 5 K increments is shown in each panel for the final 20 days of the respective simulation. The black dashed line indicates the domain and time-average precipitation value in each panel. Gray shaded regions indicate nighttime hours, while yellow shaded regions represent daytime hours with nonzero insolation. Precipitation transitions from steady state diurnal oscillations at low SST values to an episodic deluge regime by 325 K.

in the lower troposphere (see panels (b)–(d) in Figure 3) leads to strong convective inhibition and a complete shutdown of daytime convection. As SSTs further increase to 322–323 K in Figure 6, convective inhibition begins to extend into the night with precipitation remaining suppressed even during nighttime hours. By SSTs of 324–325 K, convection shifts fully to an episodic deluge regime, where the lower troposphere becomes decoupled from the upper troposphere, allowing instability to accumulate until convection is triggered (see Figure 7; discussed further below).

The mean precipitation increases steadily from 295 to 321 K but decreases at higher SSTs due to global energy balance constraints. In the global mean atmospheric energy budget, the vertically integrated net radiative heating rate is approximately balanced by mean precipitation and surface sensible heat fluxes (Jeevanjee & Romps, 2018; O'Gorman et al., 2012; Pierrehumbert, 2002; Song et al., 2023). Typically, surface sensible heat fluxes are negligible, and the net radiative heating rate is approximately balanced by latent heat release from precipitation,

$$\rho_w L P \approx \frac{-c_p}{g} \int_{P_s}^{0} (Q_R)\, dp. \tag{2}$$

Here, ρ_w is the density of water, L is the latent heat of vapourization, P is the precipitation rate, c_p is the specific heat at constant pressure, g is the gravitational acceleration, and Q_R is the net radiative heating rate. As SST increases, radiative cooling in the upper troposphere strengthens (e.g., Jeevanjee & Romps, 2018), leading to

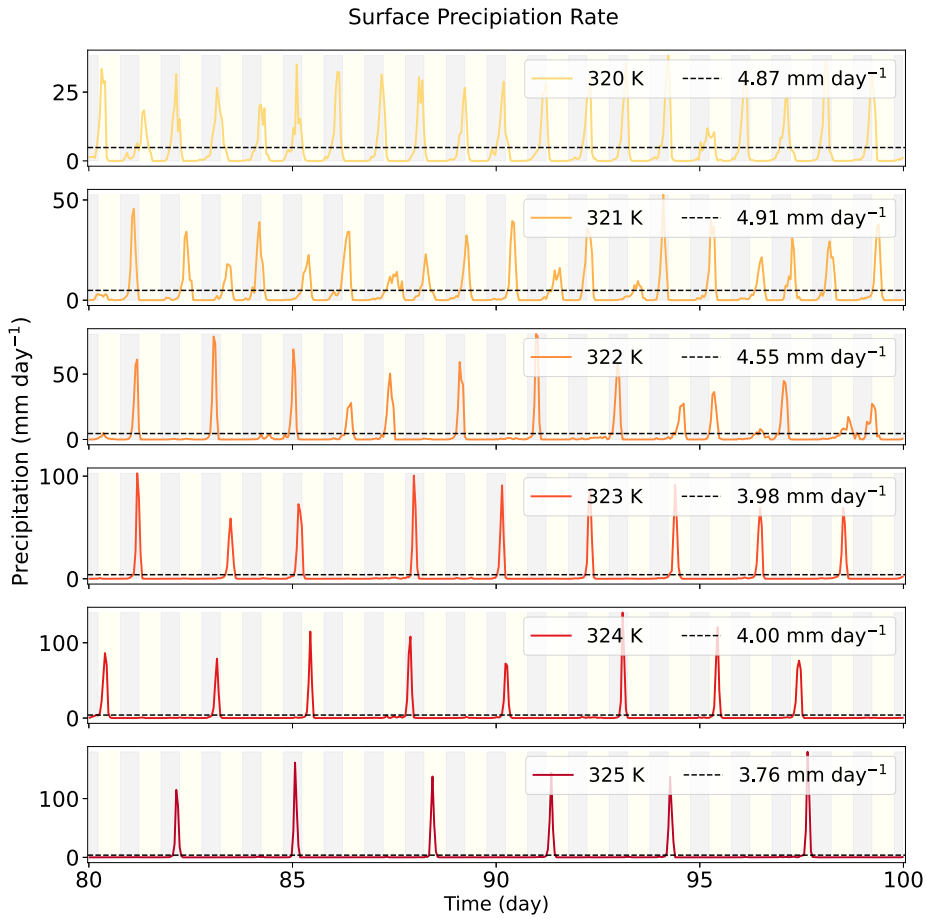

Figure 6. The domain-mean precipitation rate for RCE simulations with fixed SST from 320 to 325 K (in 1 K increments) is shown in each panel for the final 20 days of the respective simulation. The black dashed line indicates the domain and time-average precipitation in each panel. Gray shaded regions indicate nighttime hours, while yellow shaded regions represent daytime hours with nonzero insolation. Precipitation shifts from daily rain events synchronized with the diurnal oscillations at 320–321 K to a more episodic deluge regime pattern at higher surface temperatures. The duration of dry spells increases progressively from 323 to 325 K, with 325 K having about 3-day long dry-spells.

increased mean precipitation rates in the 295–320 K range simulations. Simultaneously, as SST increases, lower-tropospheric radiative cooling weakens and begins to transition to radiative warming, as shown in Figure 3a. For SSTs greater than 322 K, the mean precipitation declines due to LTRH increasing as SST increases as shown in Figure 3 (Song et al., 2023).

In this section, we focus on the radiatively driven mechanism for the transition to a RO convection regime similar to Song et al. (2023) and Seeley and Wordsworth (2021). In Section 3.3, we examine the quasi-equilibrium breakdown hypothesis and heat engine framework proposed by Spaulding-Astudillo and Mitchell (2024). Figure 7 compares the (a) latent heating, (b) potential temperature in the inhibition layer, (c) near surface moist static energy, and (d) rain rate for the 321 K (left column), 323 K (middle column) and 325 K (right column) fixed SST simulations. In the fixed SST simulations, LTRH leads to the formation of an inhibition layer in the lower troposphere, which decouples the lower troposphere from the upper troposphere.

In the 321 K simulation, precipitation is absent from the afternoon to early nighttime hours, as indicated by the near-zero latent heating throughout most of the atmospheric column (from the surface to 18 km) and zero rain rates (Figure 7, left column panels a and d), suggesting an inhibition layer is stabilizing the atmosphere against convection. The potential temperature in the inhibition layer (Figure 7b, left column) warms during the daytime due to shortwave heating of the lower troposphere (see Figure 3), while nighttime radiative cooling reduces θ_{inhibit} until the inhibition layer is broken down at the end of the nighttime hours and convection is triggered (Figure 7,

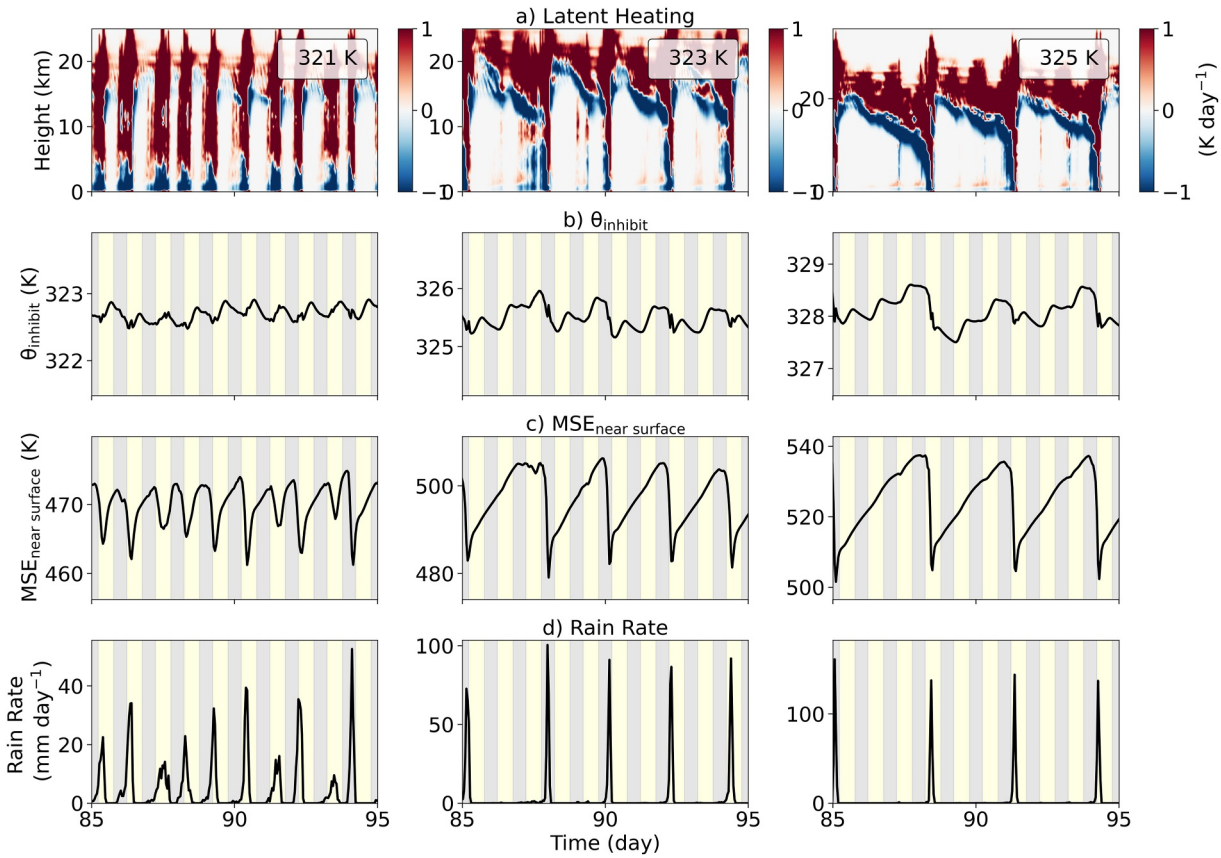

Figure 7. Time series for the 321 K (left), 323 K (middle) and 325 K (right) fixed SST simulations showing (a) latent heating (K day^{-1}), (b) potential temperature at the inhibition layer, $\theta_{inhibit}$(K), (c) moist static energy (MSE) near the surface (K), and (d) rain rate (mm day^{-1}). Gray shaded regions indicate nighttime hours, while yellow shaded regions represent daytime hours with positive insolation.

left column panels a and d). The diurnal cycle modulates precipitation, which peaks in the late night to early morning hours when the inhibition layer is weakest, corresponding to a minimum in $\theta_{inhibit}$.

As SST is increased to 323 and 325 K, the inhibition layer does not fully break down during the nighttime and convection remains suppressed. As shown in Figure 7b, $\theta_{inhibit}$ oscillates diurnally but also shows a gradual upward trend indicating progressive accumulation of inhibition in the 321 and 325 K simulations. $\theta_{inhibit}$ drops to a minimum when a rain event occurs. The diurnal oscillations in $\theta_{inhibit}$ correspond to daytime shortwave heating of the lower troposphere and nighttime cooling. However, nighttime cooling is insufficient to fully erode the inhibition layer, though it does weaken it, as evidenced by the decreasing $\theta_{inhibit}$ during nighttime hours. Over time, the lower atmospheric layer becomes warmer and increasingly stable, as shown in panel (b) and (c) of where $\theta_{inhibit}$ and near surface MSE accumulate, respectively, due to the radiative heating of this layer.

Convection is triggered when precipitation in the mid-troposphere evaporates and weakens the inhibition layer. Radiative cooling in the upper troposphere (see Figure 3) builds convective instability and leads to condensation and latent heat release in the upper atmosphere, as seen in Figure 7a. In the 321 and 325 K simulations, rain evaporates before reaching the surface, often referred to as *virga*. Virga progressively descends through the column, and eventually evaporation occurs near the top of the inhibition layer (see Figure 7a). The resulting evaporative cooling weakens the inhibition layer triggering a convective event. Once an episode of heavy rain is initiated, deep convection occurs from the surface to the upper troposphere until the instability is consumed, after which the cycle repeats.

The 321 K fixed SST case, shown in the left column of Figure 7, indicates the formation of an inhibition layer during daytime hours, with latent heating near zero and precipitation occurring only once per day. As SST increases to 323 K, shown in the middle column of Figure 7, inhibition lasts for a couple days, during which near-

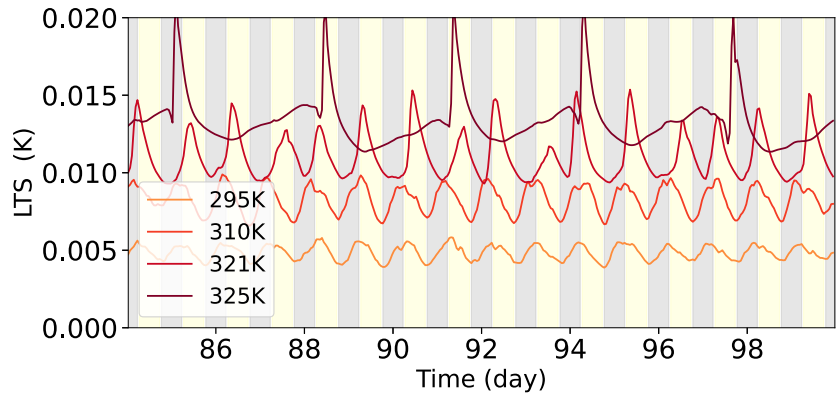

Figure 8. Time series of lower tropospheric stability (LTS) defined as the difference between θ_{inhibit} and the surface-level potential temperature. Gray shaded regions indicate nighttime hours, while yellow shaded regions represent daytime hours.

surface MSE and instability builds up until a storm is triggered. When a storm is triggered the instability is consumed by the rain through latent heating causing a sharp drop in near surface MSE and θ_{inhibit}. The potential temperature at the inhibition layer (Figure 7b) still shows diurnal variation when convection is suppressed and instability is accumulating in the 323 K case. The 325 K case, shown in right column of Figure 7, is similar to the 323 K case but with reduced frequency of rain events. Both 323 and 325 K cases suggest that even in the RO convection regime, convection is triggered when the inhibition layer is weakest, typically during the transition from late night to early morning. The diurnal cycle modulates episodic precipitation, with storm events aligning with the dawn transitions.

We show the lower tropospheric stability (LTS) in Figure 8, defined as the difference between θ_{inhibit} and the potential temperature at the surface, to compare the fixed SST simulations. Figure 8 shows a transition from LTS variations predominantly driven by diurnal fluctuations at SSTs $\leq$ 320 K to a regime where LTS variations are dominated by latent heating, coinciding with episodic precipitation events. The transition to RO convection regimes is associated with an increase in the time-mean LTS, similar to the increase in convective inhibition reported by Yang et al. (2024). During intense episodic rain events, rain consumes atmospheric instability through latent heating, causing a spike in LTS. Just prior to the rain event, virga reduces the LTS, producing a small dip in the LTS visible just before precipitation spike in the 325 K case (maroon line). This small dip coincides with a dip in θ_{inhibit} right before deep convection begins when virga evaporates near the top of the inhibition layer enabling the formation of strong convection. As SST increases, the peak of precipitation shifts from the nighttime to the early morning hours, and precipitation becomes more intense.

3.2. Slab Ocean Simulations With Diurnally Varying SST

Slab ocean simulations allow us to understand the effect of the diurnal cycle in swamp-like conditions where the SST varies diurnally rather than remaining fixed. In order to change the mean SST across the five slab ocean simulations, we vary the ocean heat flux for a fixed depth slab ocean model (see Methods). The 100 W m^{-2} simulation is initialized to balance the top-of-atmosphere energy budget for a 300 K mean SST. In this case, the mean SST remains approximately stable over time, and the troposphere has a nearly uniform radiative cooling rate. Slab ocean simulations initialized with an ocean flux less than 100 W m^{-2} warm over time while simulations with an ocean flux greater than 100 W m^{-2} cool over time. The SST evolution and mean SST for the five slab ocean simulations is shown in Figure 9. Diurnal temperature fluctuations in the slab ocean simulations are approximately 10 K. The five slab ocean simulations have mean SST temperatures of 285 K for the 150 W m^{-2}, 303 K for the 100 W m^{-2}, 319 K for the 50 W m^{-2}, 326 K for the 10 W m^{-2} and 337 K for the $-$100 W m^{-2} simulation, averaged over the last 60 days of the respective simulation. Lower ocean flux values correspond to hotter simulations. Temperatures always peak after midday and reach their minimum at the end of the nighttime. Similar to the fixed SST simulations, we first focus on the radiatively driven mechanism for the transition to RO convection (Seeley & Wordsworth, 2021; Song et al., 2023) in this section and then examine heat-engine framework of Spaulding-Astudillo and Mitchell (2024) in Section 3.3.

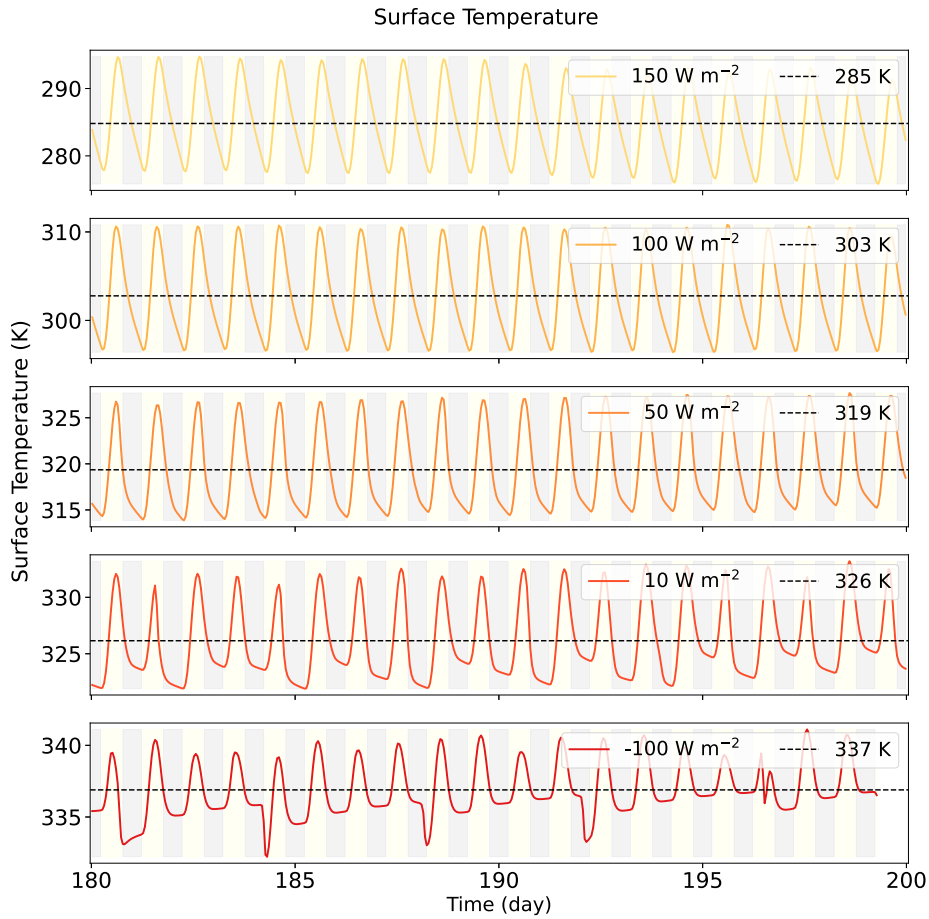

Figure 9. Domain-mean surface temperature variation in the five slab ocean RCE simulations. The slab ocean simulations represents tropical swamp-like conditions rather than an ocean through a mixed layer depth that controls the thermal inertia. Larger flux simulations cool over time while smaller flux simulations warm over time. The black dashed line shows the mean surface temperature for each simulation over that last 60 days. Gray shaded regions indicate nighttime hours, while yellow shaded regions represent daytime hours.

The diurnal temperature variations in the slab ocean simulations coincide with the net radiative heating rate trends. Figure 10a presents the mean radiative heating rate profile over the last 60 days while panels (b) and (c) show a 24 hr composites of the mean radiative heating for the 100 W m^{-2} and 10 W m^{-2} ocean heat flux simulations respectively, and panel (d) shows their difference (10 W m^{-2} - 100 W m^{-2}). Figure 10b and c show nighttime radiative cooling and strong daytime radiative heating in the mid and lower troposphere. Nighttime radiative cooling continuously decreases the lower tropospheric temperature throughout the night, reaching a minimum at dawn, whereas daytime shortwave heating increases the temperature, peaking at end of the daytime (see Figure 9). Panel (d) shows that the 10 W m^{-2}, hotter simulation, has weaker nighttime radiative cooling and stronger daytime radiative heating. The 150 W m^{-2} and 100 W m^{-2} slab ocean simulations have nearly constant lower tropospheric radiative cooling, shown in Figure 10a. However, as ocean heat flux is decreased, mean SST is increased, upper troposphere radiative cooling intensifies while lower tropospheric radiative cooling transitions to weak radiative warming as in the fixed SST simulations. Overall, Figure 10 shows that as mean SST increases in the slab ocean simulations, lower tropospheric daytime radiative warming increases but nighttime cooling decreases, causing the time-mean net radiative heating rate to transition from lower tropospheric cooling to weak heating.

Figure 11 shows the (a) latent heating, (b) potential temperature of the inhibition layer taken as the average θ between 390 and 1,600 m, (c) near surface moist static energy, and (d) the rain rate over the final 20 days of the baseline 100 W m^{-2} simulation. All variables show diurnal oscillations. Both the latent heating (Figure 11a) and

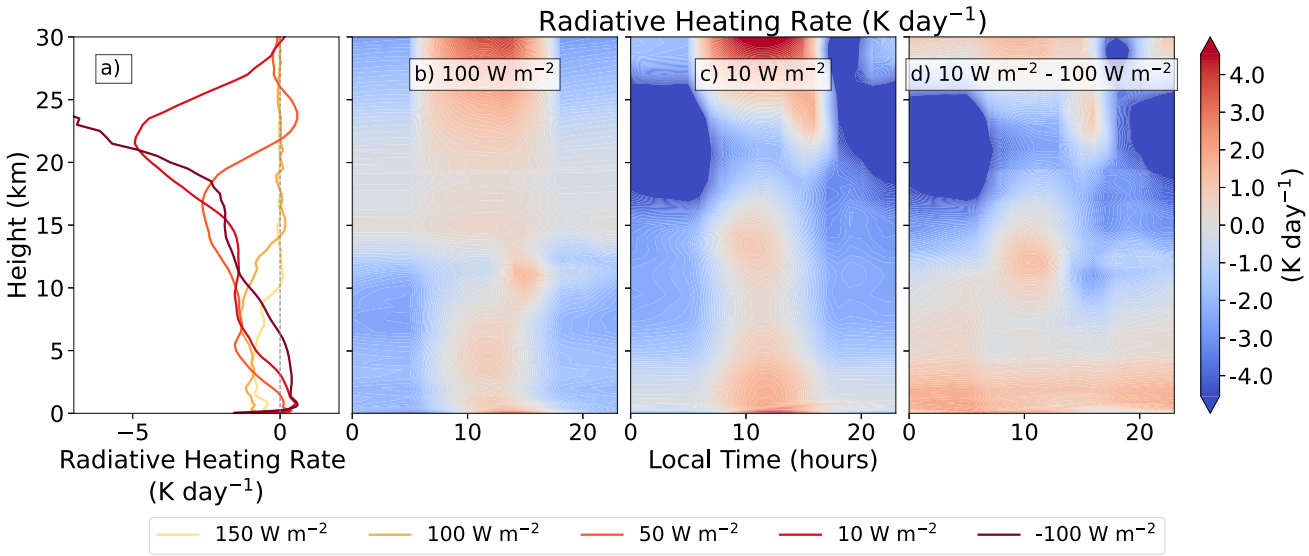

Figure 10. Daily averaged composite of radiative heating rate (K day^{-1}) as a function of height (km) and local time (hours) for (b) 100 W m^{-2}, (c) 10 W m^{-2} ocean heat flux simulations, and (d) their difference. The radiative heating rate composites show stronger daytime heating and weaker nighttime cooling in the lower troposphere of the 10 W m^{-2} simulation relative to the 100 W m^{-2} simulation. Panel (a) shows the time and domain-averaged radiative heating rate (K day^{-1}) profiles for the slab ocean simulations using ocean heat flux values of 150 W m^{-2} (yellow), 100 W m^{-2} (orange), 50 W m^{-2} (red-orange), and 10 W m^{-2} (red) and −100 W m^{-2} (maroon). At higher ocean heat flux rates, no lower-tropospheric radiative heating (LTRH) is observed. However, as the ocean heat flux decreases to 50 W m^{-2} and below, LTRH begins to develop.

rain rate (Figure 11d) show precipitation occurs once daily, but unlike the 300 K fixed SST simulation, convection is nearly fully suppressed during the late nighttime to early morning hours.

During the nighttime, longwave cooling in the lower troposphere reduces θ_{inhibit} (Figure 11b) which leads to increased static stability that suppresses convection. The stable layer is weakened and breaks down during the daytime due to shortwave heating of the surface (see Figure 9) which leads to moistening of the lower troposphere, and causes the near surface MSE to increase (Figure 11c). Convection occurs in the afternoon and early evening when the inhibition layer (see Figure 11b) is the weakest and diurnal warming is the largest (see Figure 9). When moist convection occurs, near surface MSE remains approximately constant as seen in Figure 11c. Figure 11d shows daily rain events that occur in the afternoon to early evening hours, which is in agreement with expectations for diurnal modulation of precipitation over tropical land (Bechtold et al., 2004). Additionally, in Figure 11d, the peak intensity of the rain rate is larger than the 300 K fixed SST simulation (see Figure 5) due to the variation in mean SST in the slab ocean simulation.

Figure 12 shows the domain-mean precipitation rate time series over the last 20 days for the five slab ocean simulations and the time-mean precipitation rate as the black dashed line. At 100 W m^{-2} (mean SST 303 K) and 150 W m^{-2} (mean SST 286 K) precipitation primarily occurs in the late afternoon early evening but small amounts of precipitation can occur during the nighttime and early morning hours. At the slab ocean flux of 150 W m^{-2} more heat is removed from the surface compared with the stable 100 W m^{-2} case, leading the mean SST to cool over time (see Figure 2). In this simulation, the lower mean SST leads to a weaker radiative cooling rate and lower global mean precipitation relative to the 100 W m^{-2} case (see Figure 10a).

Conversely, reducing the flux to 50 W m^{-2} increases mean precipitation relative to the 100 W m^{-2} case due to an increase in the mean SST to 318 K and stronger longwave cooling of the atmosphere (see Figure 10). Additionally, in the 50 W m^{-2} simulation, precipitation peaks once daily with no convection in between. In the 10 W m^{-2} case the mean precipitation decreases compared to the 50 W m^{-2} case due to an increase in LTRH (see Figure 10), which begins to decouple the surface from upper troposphere. In this case, RO convection and episodic precipitation begin to form. At −100 W m^{-2}, there is a clear transition to strong RO convection, characterized by infrequent rain events and dry spells lasting up to three days.

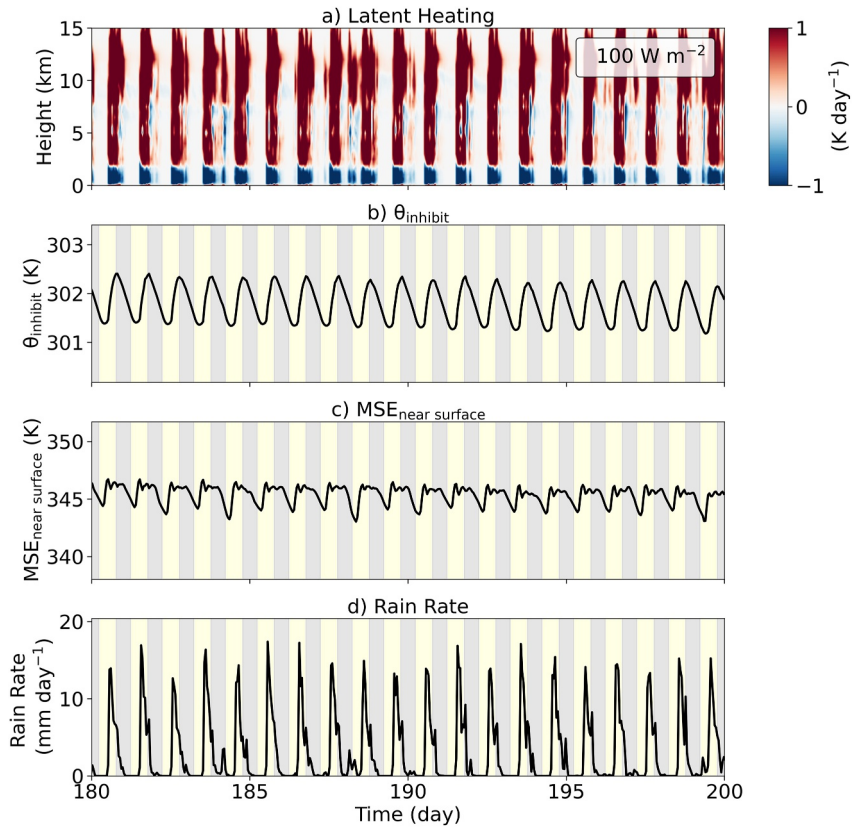

Figure 11. Time series for the 100 W m^{-2} slab ocean simulation showing (a) latent heating (K day^{-1}), (b) potential temperature at the inhibition layer (K), (c) moist static energy (MSE) near the surface (K), and (d) rain rate (mm day^{-1}). Gray shaded regions indicate nighttime hours, while yellow shaded regions represent daytime hours with positive insolation.

The global mean precipitation trends can be understood through Figure 10a which shows the net radiative heating rates for each simulation averaged over the last 60 days. The 100 and 150 W m^{-2} simulations show radiative cooling in the lower troposphere but as the ocean heat flux is reduced, and the SST increases, the LTRH increases leading to a reduction in the vertically integrated radiative heating rate and global mean precipitation in agreement with Equation 2.

Figure 13 compares the 50, 10 and −100 W m^{-2} slab ocean simulations to highlight simulations within a steady state convection regime (50 W m^{-2}), transitioning to an RO convection regime (10 W m^{-2}), and fully within the RO convection regime (−100 W m^{-2}). In the 50 W m^{-2} case (mean SST 319 K) convection is completely suppressed in the late night to midday hours indicated by the zero precipitation in Figure 13d, but inhibition is not yet strong enough to suppress convection in the afternoon or early evening hours. The 50 W m^{-2} shows similar trends to the baseline 100 W m^{-2} simulation where as temperature increases from dawn to dusk, the near surface moist static energy and $\theta_{inhibit}$ increase due to shortwave warming of the near surface layer that promotes convection and precipitation. Both $\theta_{inhibit}$ and the near surface MSE oscillates with diurnal variations, but Figure 13a and d show that nighttime stabilization against convection is stronger in the 50 W m^{-2} simulation compared to the 100 W m^{-2} simulation as precipitation and latent heating are completely suppressed from midnight to midday.

Further reduction of the ocean heat flux to 10 W m^{-2} (mean SST 326 K) increases convective stabilization during the night, which becomes strong enough to start inhibiting convection during the daytime hours. At 10 W m^{-2}, we begin to observe the transition to RO convection regime in Figure 13. The diurnal cycle still modulates precipitation to occur during dusk transition from late afternoon to early evening hours as expected for diurnal modulation of precipitation over land. At ocean heat flux of −100 W m^{-2}, representing convergence of energy into the domain, convection is completely suppressed during extended day-long periods and convection occurs

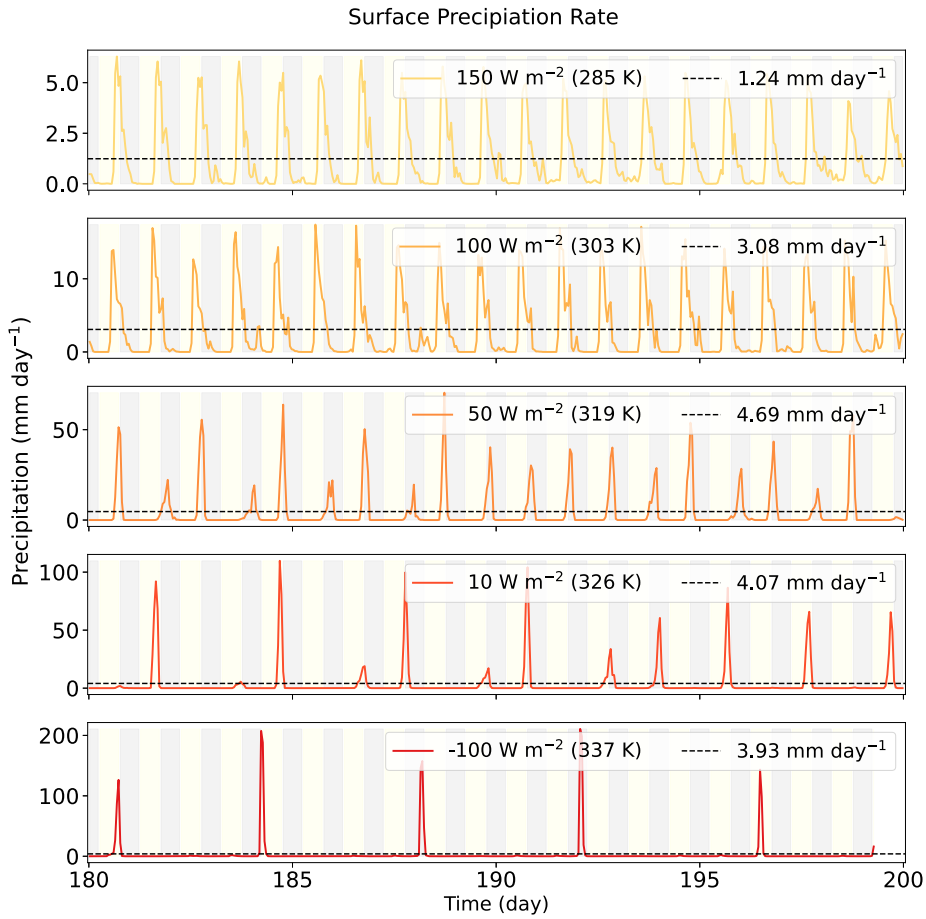

Figure 12. Domain-mean precipitation rate for the five slab ocean RCE simulations. The slab ocean simulations represent tropical swamp-like conditions where mean surface temperatures varies and larger flux simulations cool over time while smaller flux simulations heat over time. The black dashed line shows the mean precipitation rate for each simulation. Precipitation oscillates due to diurnal variations in 50–150 W m^{-2} simulations. However, around 50 W m^{-2} convection is completely suppressed during parts of the day and below 10 W m^{-2} precipitation transition to RO convection regime.

when the inhibition layer is the weakest during late night to morning hours or dawn transitions similar to the fixed SST simulations.

Overall the slab ocean simulations show the transition to a RO convection regime occurs in the 10 W m^{-2} with a mean SST of 326 K. Initially, in the RO convection regime, the diurnal cycle modulates precipitation to occur in the late afternoon to early evening hours as expected for diurnal precipitation patterns in swamp-like conditions. However, as mean SST increases, the diurnal cycle modulates precipitation to occur at the dusk transition as in the fixed SST simulations.

3.3. Alternative Mechanisms for the Emergence of RO Convection Regimes

3.3.1. The Quasi-Equilibrium Breakdown Hypothesis

Thus far, we have examined the transition to an RO convection regime through a radiatively driven perspective. In the preceding sections, we show that in the RO regime, LTRH creates an inhibition layer that decouples the lower and upper atmosphere, suppressing convection for multiple days. Convection is triggered when radiative cooling in the upper troposphere generates virga that descends down through the atmosphere and evaporates at the top of the inhibition layer. We have also demonstrated how these processes are modulated by diurnal radiative variability. This interpretation for the transition to RO convection is in agreement and aligns with previous studies of RO convection (e.g., Dagan et al., 2023; Dagan & Eytan, 2024; Seeley & Wordsworth, 2021; Song et al., 2023).

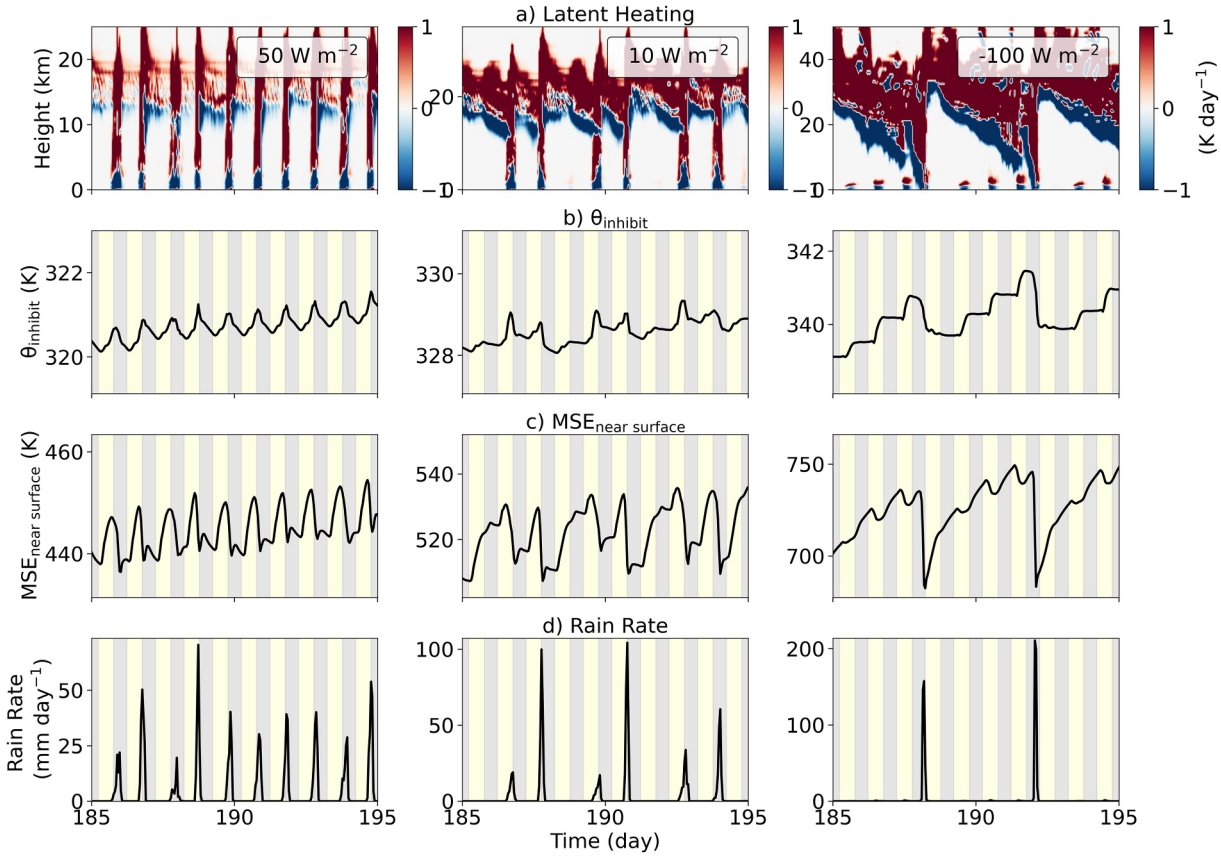

Figure 13. Time series for the 50 W m^{-2} (left), 10 W m^{-2} (middle), and −100 W m^{-2} (right) slab ocean simulations showing (a) latent heating (K day^{-1}), (b) potential temperature at the inhibition layer (K), (c) moist static energy (MSE) near the surface (K), and (d) rain rate (mm day^{-1}). Gray shaded regions indicate nighttime hours, while yellow shaded regions represent daytime hours with positive insolation.

However, there is an alternative mechanism to explain the transition to RO convection regimes. In the *quasi-equilibrium (QE) breakdown hypothesis*, derived in full detail by Spaulding-Astudillo and Mitchell (2024), radiative convective equilibrium is modeled as a heat engine where the atmosphere converts the net radiative heating into work through a thermodynamic efficiency. The thermodynamic efficiency represents the loss in the rate of work or entropy due to irreversible processes. QE convection breaks down and transitions to RO convection when the mass flux from the lower to upper troposphere is insufficient to meet the energy demand of the heat engine (Spaulding-Astudillo & Mitchell, 2024). This is approximated by assuming that there is no net vertical transport of mass, and thus QE breakdown occurs when,

$$\eta \Delta h > \text{CAPE} \tag{3}$$

where η is the heat engine efficiency, Δh is the difference in the moist static energy (MSE) between the surface and tropospheric minimum, and CAPE is the convective available potential energy which represents the work the atmosphere exerts to lift an air parcel adiabatically. The heat engine efficiency, when the only source of entropy generation is frictional dissipation, is given by,

$$\eta = T_d \left(\frac{1}{T_a} - \frac{1}{T_s} \right), \tag{4}$$

where T_d is the temperature at which frictional dissipation occurs, T_a is the temperature at which radiation is emitted from the atmosphere, and T_s is the temperature at which radiation is absorbed at the surface. Following

Spaulding-Astudillo and Mitchell (2024), the frictional dissipation is assumed to occur between the surface and the radiative emission level, such that

$$T_d = \frac{Ts + Ta}{2}. \tag{5}$$

The QE-breakdown condition, given by Equation 3, can be evaluated using convection-resolving simulation output or predicted theoretically using the zero buoyancy model (ZBM) to analytically determine the CAPE and Δh. The ZBM assumes that clouds are exactly neutrally buoyant with respect to their environment (Singh & O'Gorman, 2013). The ZBM is derived and discussed in detail in a few publications (e.g., Romps, 2016; Seeley & Romps, 2015; Singh & O'Gorman, 2013) and here, we only present the equations required to determine CAPE and Δh to evaluate the QE-breakdown hypothesis.

To begin, the vertical derivative of moist static energy is,

$$\partial_z h^* = -\frac{a}{1+a}\gamma L q^*, \tag{6}$$

where a is the non-dimensional entrainment or bulk plume parameter, $\gamma \equiv \partial_z \ln q^*$ is the vertical moisture lapse rate, L is the latent heat of vapourization, and q^* is the saturation vapor mixing ratio. γ is given by,

$$-\gamma = \frac{g}{R_a T} - \frac{L\Gamma}{R_v T^2}, \tag{7}$$

where g is gravitational acceleration, R_a and R_v are the gas constants for dry air and water vapor respectively, T is temperature, L is the latent heat of vapourization, and $\Gamma = -\partial_z T$ denotes the temperature lapse rate. The temperature lapse rate set by entraining convection, $\Gamma \equiv -\partial_z T$ is

$$\Gamma = \frac{g}{c_p}\left[\frac{1 + a + q^* L/(R_a T)}{1 + a + q^* L^2/\left(c_p R_v T^2\right)}\right]. \tag{8}$$

Lastly, CAPE is given by

$$\mathrm{CAPE} = \int B dz \approx \int_{z_{\mathrm{LFC}}}^{z_{\mathrm{LNB}}} g\,\frac{T - \overline{T}}{\overline{T}}\,dz, \tag{9}$$

where z_{LFC} and z_{LNB} are the heights of the level of free convection and the level of neutral buoyancy, respectively, T is the parcel temperature determined by solving Equation 8 with $a = 0$, and $\overline{T}$ is the environmental temperature. The bulk plume parameter, a, represents the amount of entrainment in the system. When $a = 0$, there is no entrainment and the environment lapse rate is equal to the moist adiabat. Conversely, with more entrainment, $a \to \infty$, the environment lapse rate approaches the dry adaibat (Romps, 2016).

Technically, CAPE should be determined using the virtual temperature as density variations due to compositional gradients can affect CAPE (Emanuel, 1994). However, virtual effects are neglected in the derivation for the QE-breakdown hypothesis in Spaulding-Astudillo and Mitchell (2024) and thus neglected in the theoretical calculation of the QE-breakdown hypothesis in this work. Virtual effects are typically small and reasonably neglected for Earth climate at low SSTs but become important at higher SSTs, and in planetary studies, especially when considering low mean molecular weight atmospheres (e.g., Habib & Pierrehumbert, 2024; Habib & Pierrehumbert, 2025; Seeley & Wordsworth, 2025).

To test the QE-breakdown hypothesis, we evaluated the QE condition given by Equation 3 using the RCE simulation outputs for an "experimental" prediction and by solving Equations 3–9 to get a theoretical prediction in a similar manner to Spaulding-Astudillo and Mitchell (2024).

For the theoretical prediction of the QE-breakdown hypothesis, CAPE and Δh are computed using the ZBM framework given by Equations 6–9, η is taken to be the same as the experimental value, and a fixed value is used

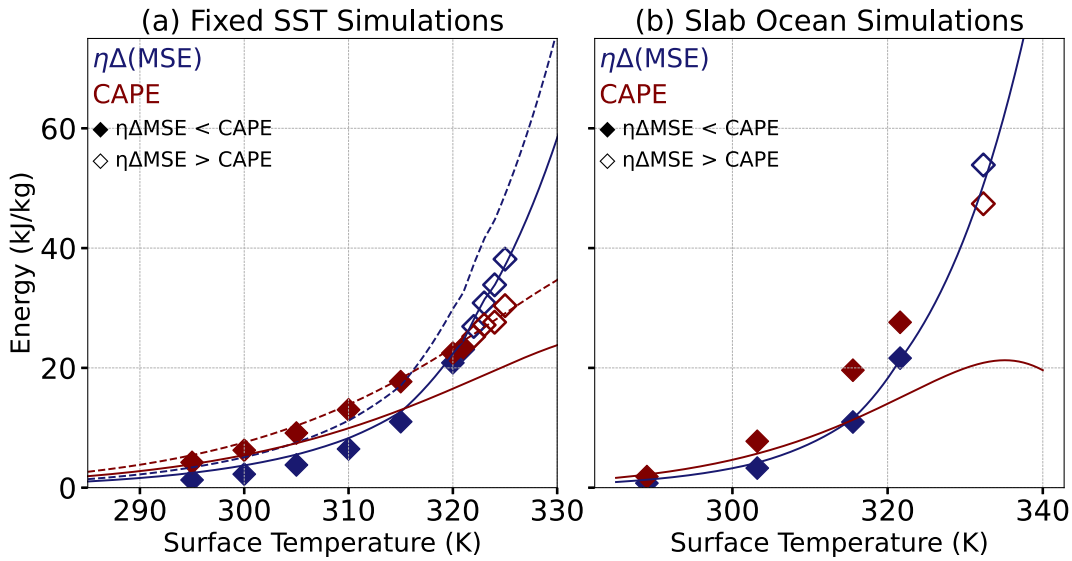

Figure 14. Quasi-Equilibrium Condition for the (a) fixed SST simulations and (b) slab ocean RCE simulations. Diamond markers represent points determined using the respective RCE simulation output and solid lines show predictions using the analytical theory presented in Section 3.3. Open diamond markers indicate points where the QE-breakdown hypothesis predicts RO convection. Red points and line indicate the estimation for CAPE and blue points and lines show the $\eta\Delta h$. In panel (a) solid lines use a bulk plume parameter of 0.5 while dashed lines use 0.85. In panel (b), the bulk plume parameter is set to 0.4.

for the bulk plume parameter, a. As it is difficult to estimate the heat engine efficiency without simulation data, we use the same η for both the experimental and theoretical calculations. η was determined by using Equation 4 with the surface temperature for the respective simulation, and the average T_a over the last 40 days T_a was determined by taking the temperature where the temperature profile became isothermal. Additionally, since we didn't have complete simulation output for calculating the bulk plume parameter, we tested different values for a and used the values that best fit the simulation results. Note that the bulk plume parameter is only needed for the theoretical prediction of CAPE and Δh for the QE condition.

To evaluate the theoretical CAPE, we solve Equations 8 and 9 following (Romps, 2016) using the height profile, time-mean surface temperature, surface pressure, and a tropospheric proxy T_{trop} taken as the temperature where the time-mean temperature profile became approximately isothermal from the respective simulations (same as T_a). Similarly to evaluate the theoretical moist static energy, we evaluate Equations 6–8 following (Romps, 2016) using the time-mean surface temperature, surface pressure, the model top height, and the mass weighted tropospheric relative humidity computed from the simulation outputs.

For the experimental prediction of the QE-breakdown hypothesis, CAPE, Δh, and η were directly computed using the RCE simulation outputs. CAPE was determined using Equation 9 with the virtual temperature output from the RCE simulations. We opted to add virtual effects in the experimental prediction as it did not complicate the calculation and it improves accuracy. Using virtual temperature slightly increases the CAPE for SSTs >310 K and shifts the QE threshold to higher SSTs. With a larger CAPE value for the same $\eta\Delta$MSE, a higher SST is needed to satisfy $\eta\,\Delta h > \text{CAPE}$ criterion. For instance, we find in the fixed SST simulations calculating CAPE without virtual effects suggests episodic convection should emerge at about 318 K, while including virtual effects shifts the threshold to approximately 322 K (not shown). Δh was determined by directly using the MSE output from the simulations and taking the difference between the MSE at the surface and the minimum tropospheric MSE value, $\Delta h = h_s - h_{\text{min}}$. Both CAPE and Δh were averaged over the last 40 days for each simulation in the fixed SST simulations and 60 days for the slab ocean simulations.

Figure 14 shows the QE-breakdown hypothesis for the fixed SST simulations in panel (a) and the slab ocean simulations in panel (b). Diamond markers represent points determined using RCE simulation output and lines show predictions using the analytical theory presented above. Open diamond markers indicate points where the QE-breakdown hypothesis predicts RO convection. Red points and lines indicate estimation for CAPE and blue

points and lines show the $\eta\Delta h$. In panel (a), the solid lines indicate theoretical CAPE and $\eta\Delta h$ calculated with $a = 0.5$, while the dashed line uses $a = 0.85$. For the slab ocean simulations in panel (b), $a = 0.4$.

For the fixed SST simulations in Figure 14a, the RCE simulation results (diamond points) show the QE condition is satisfied at 322 K when $\eta\Delta h$ exceeds the CAPE and the transition to RO convection should occur at SSTs greater than 322 K. This is in agreement with the fixed SST simulations which showed the emergence of RO convection around 323 K, and in agreement with the findings presented by Spaulding-Astudillo and Mitchell (2024).

The theoretical prediction (solid lines in Figure 14a) for the QE-breakdown hypothesis broadly agrees with the empirical prediction for the emergence of RO convection (diamond points in Figure 14), but the theoretical calculation shows more variance due to assumptions and uncertainties in the calculation. For $a = 0.5$ (solid lines), the theoretical prediction reproduces the simulated $\eta\Delta h$ output, but under-predicts the CAPE once the SSTs exceed 300 K. Raising the bulk plume parameter to $a = 0.85$ (dashed lines), brings the theoretical profile into much closer agreement with the simulated CAPE, but at the cost of substantially over-predicting $\eta\Delta h$. Regardless of which bulk plume value is chosen, the theory places the transition to RO convection at an SST of about 315 K which is slightly lower than what is observed within the RCE simulations.

The slab ocean simulations in Figure 14b also show broad agreement with the QE-breakdown hypothesis. The simulation outputs (diamond points in Figure 14b) only satisfy the QE condition given by Equation 3 when the mean SST is 337 K for the -100 W m^{-2} simulation. The transition toward a RO convection state was observed in the 10 W m^{-2} simulation which has a mean SST (over the last 60 days) of 326 K, and the QE-breakdown hypothesis shows the CAPE and $\eta\Delta h$ are close for this simulation. As with the fixed SST simulations, the theoretical prediction (solid lines in Figure 14b) under-predicts the transition to RO convection regardless of the bulk plume parameter. With $a = 0.4$, the theoretical $\eta\Delta h$ matches the simulation outputs well but significantly under predicts CAPE. The theoretical model for the slab ocean simulations suggests the emergence of RO convection at around 317 K. A key caveat for applying the QE-breakdown hypothesis to the slab-ocean simulations is that the slab ocean cases are still evolving and have not reached equilibrium, and therefore the QE condition could change with time.

The theoretical model makes a few assumptions that might impact its ability to predict the emergence of RO convection. A full discussion of the assumptions and limitations of the QE-breakdown hypothesis are discussed in Spaulding-Astudillo and Mitchell (2024). Here we highlight a few assumptions that may be impacting the results presented in Figure 14. First, there is substantial uncertainty in the bulk plume parameter. We were unable to diagnose the bulk plume parameter from the simulations, and therefore used a fixed approximation. However, the bulk plume parameter could vary between simulations (i.e., different values for each diamond point in Figure 14) which could improve the theoretical prediction for the temperature at which RO convection emerges in the.

QE-breakdown framework. Additionally, virtual effects are neglected within the theoretical prediction of the QE-breakdown model. The simulation CAPE output was calculated using the virtual temperature profile, but the theoretical CAPE prediction neglects virtual effects in its derivation. At higher SSTs, the troposphere will contain more moisture and virtual effects will become important. This could be a potential reason why the theoretical CAPE deviates from the simulation CAPE points at higher SST values in Figure 14a with $a = 0.5$ shown by the solid line.

Furthermore, the QE-breakdown theory neglects convective inhibition. In the preceding results sections, we find that convective inhibition plays an essential role in the RO convection mechanism. Future work should consider the role of convective inhibition (e.g., Yang et al., 2024) in addition or instead of CAPE in the emergence of RO convection regimes. Without the inhibition layer, convection should occur continuously as suggested by the baseline simulations for both the fixed SST and slab ocean cases.

The main goal of this work is to asses and understand how the diurnal cycle influences both the emergence and the behavior of RO convection regimes. The QE-breakdown hypothesis only predicts the critical temperature at which RO convection should occur. When we separate the simulations into daytime and nighttime segments, the prediction for the temperature at which RO convection changes little, and diurnal variations appear to have no appreciable impact in the QE-breakdown hypothesis (not shown).

Radiation is an important aspect of the QE heat engine model as the radiative heating rate is the key driver of the heat engine. Due to the simplicity of the model, the effects of radiation are condensed. The radiative heating rate

explicitly determines the efficiency of the heat engine through both the surface temperature and T_a. Additionally, radiative effects would implicitly impact the Δh term as radiation would impact the temperature profile and affect the column MSE. The QE heat-engine model offers a fast, zero-dimensional estimate of when RO convection should emerge, but its simplicity comes at a cost: all vertical structure and temporal variability are collapsed into a single mean state. This simplification likely explains why the theoretical model predicts nearly identical behavior for the slab ocean and fixed SST simulation sets, given that the main difference between these two setups is the diurnally varying, time-evolving, surface temperatures.

To emphasize, the RCE simulation outputs for both the fixed SST and slab ocean simulations, shown by the diamond markers in Figure 14, agree with the QE-breakdown hypothesis. RO convection emerges at 322 K for the fixed SST simulations and around 337 K for the slab ocean simulations, in broad agreement with the simulations. Therefore, the experimental prediction of the QE-breakdown hypothesis does capture the difference in radiative forcing between the slab ocean and fixed SST simulation sets, and its impact on the transition from steady state to episodic convection.

3.3.2. The Predator-Prey Model

We test the low-order simple "Predator-Prey" model presented by Yang et al. (2024). The Predator-Prey model provides a minimal framework for understanding the transition of steady state to RO convection regimes by modeling convective inhibition (CIN) and precipitation. Within this framework, precipitation and CIN are modeled as a system of two ordinary differential equations where; CIN is generated by subsidence from precipitation and decays exponentially over time, and precipitation is generated by convective triggers and is throttled by convective inhibition and self-limiting momentum dampening (Yang et al., 2024). In this framework, CIN and precipitation are tightly coupled where CIN suppresses rain, while rain builds CIN.

We evaluate the Predator-Prey framework using the simulation output for both the fixed SST and slab ocean simulations in Figures 15 and 16, respectively. Figures 15 and 16 shows the (a) maximum precipitation minus time-mean precipitation ($P_{\max} - \bar{P}$) versus time-mean CIN ($\overline{\text{CIN}}$), (b) the oscillation period versus the time mean CIN ($\overline{\text{CIN}}$), (c) the oscillation period versus the maximum precipitation minus the time-mean precipitation ($P_{\max} - \bar{P}$) (d) time-mean precipitation versus time-mean CIN, (e) time-mean CIN versus SST, (f) time-mean precipitation ($\bar{P}$) versus SST, (g) σ versus SST, and (f) oscillation period versus SST. σ represents the relative dispersion and is defined as the ratio of the standard deviation of the precipitation rate over the mean precipitation. Previous work (Dagan et al., 2023; Yang et al., 2024) used η rather than σ to denote the relative dispersion, but we use σ to avoid confusion with the QE-breakdown model.

Previous studies (Dagan et al., 2023; Yang et al., 2024) have used $\sigma \approx 1$ as a threshold for large variations in the precipitation rate, and as an indicator of the transition to an oscillatory convection regime. However, in our study, we have diurnal variations in precipitation and thus σ should be larger compared to convection-resolving simulations without diurnal variations. In panel (g) we plot σ to determine where the transition between steady and oscillatory convection regime should be based on where σ begins to increase more rapidly with SST. We estimate $\sigma \approx 1.8$ for the fixed SST simulations and $\sigma \approx 3.0$ for the slab ocean simulations. Values with $\sigma < 1.8$ for the fixed SST simulations and $\sigma < 3.0$ for the slab ocean simulations are shown in orange in the figure, representing steady state convection regime, whereas values greater than the threshold, shown in blue, represent RO convection regime.

Generally, we find trends similar to those presented in Yang et al. (2024). CIN increases with the surface temperature due to an increase in the radiative heating of the lower troposphere. However, simulations in the episodic convection regime show a slower increase in CIN. The mean precipitation initially increases in the steady state regime but decreases when convection transitions to an episodic regime. We find a transition in the convection regime when time-mean CIN reaches about 8 J kg^{-1} for both the fixed SST and slab ocean simulations. This value is similar to the 9 J kg^{-1} time-averaged CIN value reported by Yang et al. (2024) for their fixed SST simulation set, and in agreement with the transition from steady state to oscillatory precipitation predicted by their simple low-order model. At CIN values greater than 8 J kg^{-1} the period sharply increases, and the mean precipitation decreases suggesting the transition from steady state to episodic convection. In Figures 15 and 16, simulations represented by blue points which the Predator–Prey model predicts to be in the RO regime, do show the episodic convection trends in their precipitation timeseries.

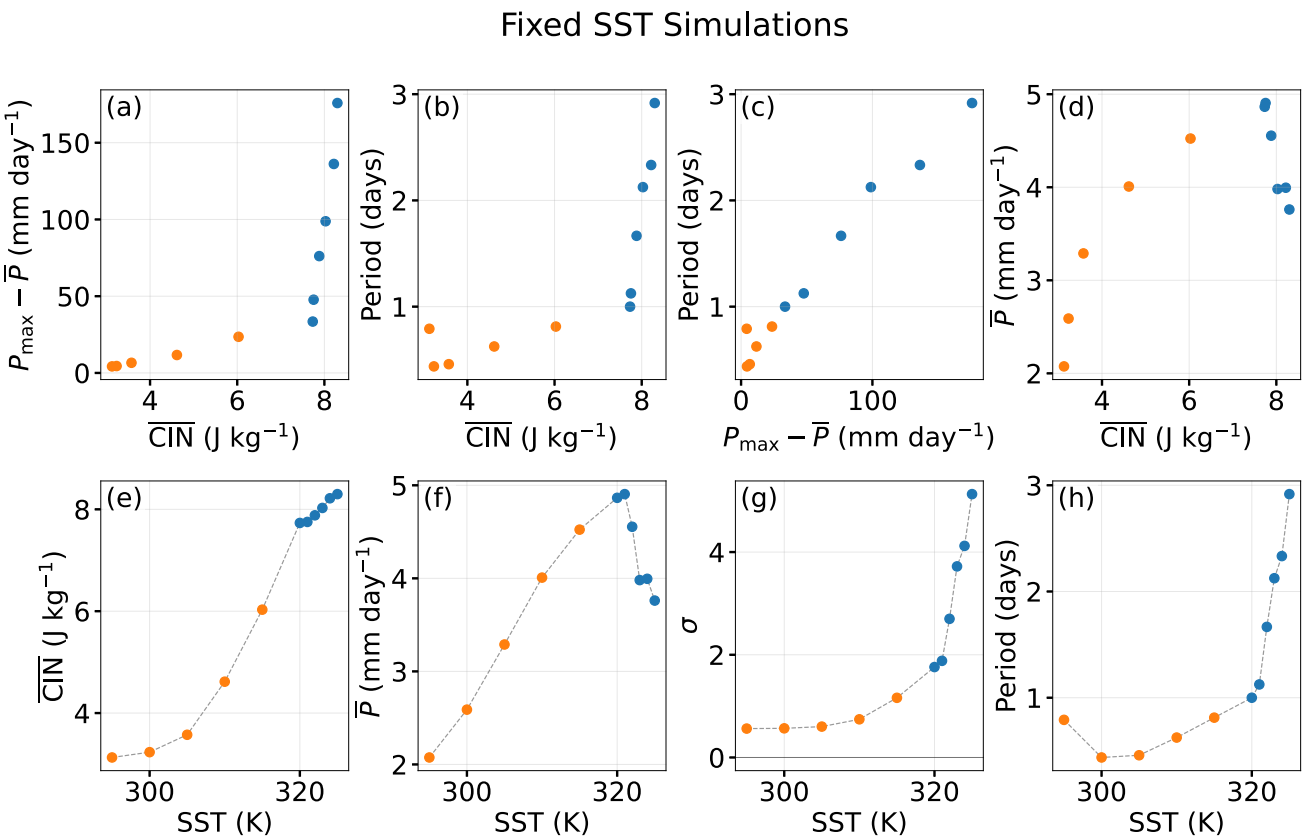

Figure 15. Predator Prey Model for the transition to RO convection regime for the fixed SST simulations showing (a) maximum precipitation (P_{max}) minus time-mean precipitation ($\bar{P}$) versus time-mean CIN ($\overline{CIN}$), (b) the oscillation period versus time-mean CIN, (c) the oscillation period versus the maximum precipitation minus the time-mean precipitation (d) time-mean precipitation versus time-mean CIN, (e) time-mean CIN versus SST, (f) time-mean precipitation versus SST, (g) σ versus SST, and (f) oscillation period versus SST. σ represents the relative dispersion and is defined as the ratio of the standard deviation of the precipitation rate over the mean precipitation. Orange points represent steady state values while blue points represent cases in the oscillatory convection regime. An overbar denotes the time-mean variable.

The Predator-Prey model provides a framework to understand the transition to RO convection regimes by understanding the CIN and its effect on precipitation, and vice versa. This model framework is agnostic of the mechanisms creating the CIN (i.e., greenhouse gases absorbing aerosols, etc.), and without simulation diagnostics to constrain the model parameters it is difficult to theoretically predict the emergence of RO convection. However, the generalized nature of the Predator-Prey model allows comparisons across different simulation setups, and could be applied to better understand RO convection regimes that arise due to diverse mechanisms, such as radiative-driven inhibition layers due to a warming climate, radiative heating due to absorbing aerosols (e.g., Dagan & Eytan, 2024), or compositional gradients in low mean molecular weight atmospheres (e.g., Habib & Pierrehumbert, 2025; Seeley & Wordsworth, 2025).

4. Conclusions

In this study, we explore the effect of diurnal variations on precipitation from present-day quasi-steady convection to hothouse, relaxation-oscillator (RO) convection regimes through two sets of small-domain RCE simulations. First, we used fixed SST RCE simulations from 295 to 325 K with open ocean boundary conditions. The fixed SST simulations showed that the diurnal cycle modulates precipitation to occur during the late-night to early morning hours. As SST is increased, precipitation transitions from peaking once daily to an episodic deluge regime at SSTs greater than 322 K where precipitation occurs once every 2–3 days in agreement with previous studies (Seeley & Wordsworth, 2021; Song et al., 2023).

Second, we used RCE simulations initialized with a slab ocean model and a shallow mixed-layer depth to mimic swamp-like conditions, allowing the mean surface temperature to fluctuate due to diurnal variations. In the slab

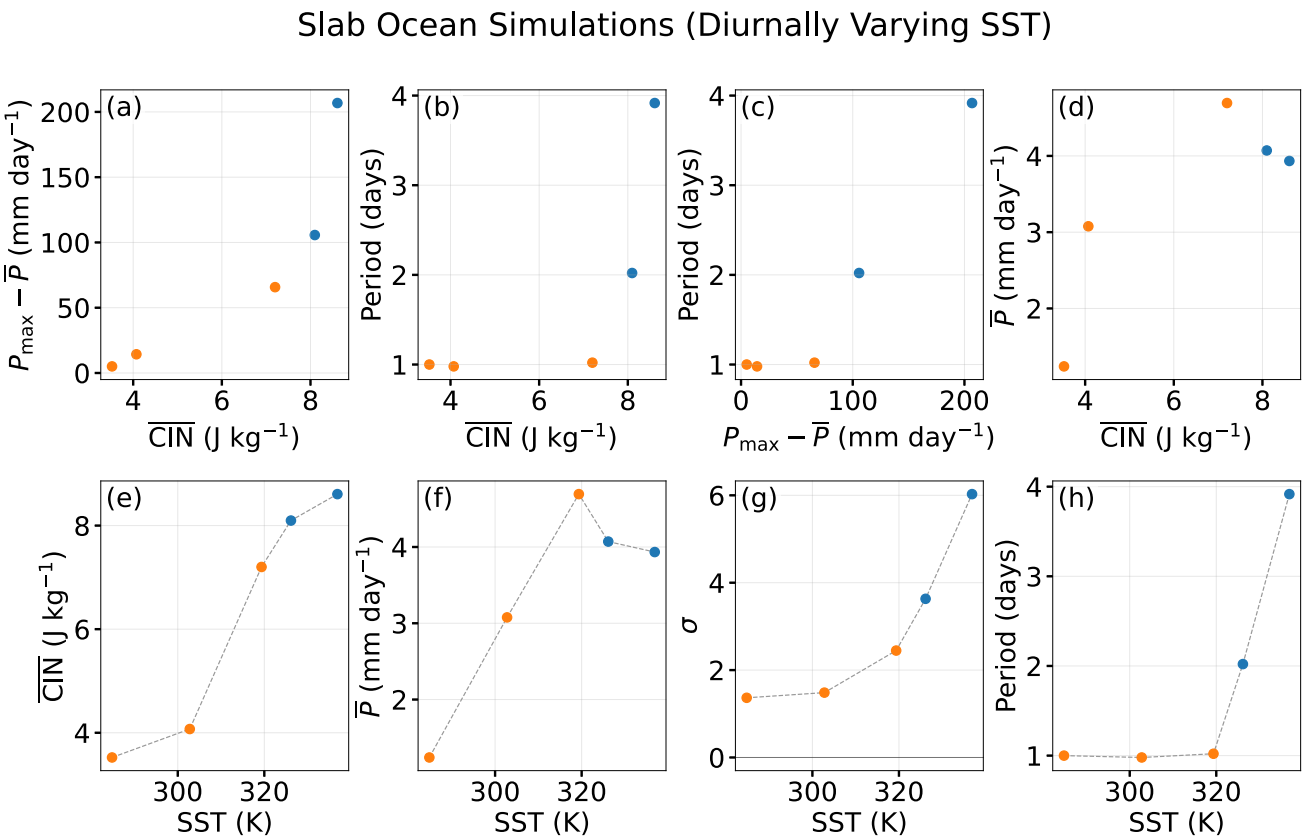

Figure 16. Predator Prey Model for the transition to RO convection regime for the slab ocean simulations showing (a) maximum precipitation (P_{max}) minus time-mean precipitation ($\bar{P}$) versus time-mean CIN ($\overline{CIN}$), (b) the oscillation period versus time-mean CIN, (c) the oscillation period versus the maximum precipitation minus the time-mean precipitation (d) time-mean precipitation versus time-mean CIN, (e) time-mean CIN versus SST, (f) time-mean precipitation versus SST, (g) σ versus SST, and (f) oscillation period versus SST. σ represents the relative dispersion and is defined as the ratio of the standard deviation of the precipitation rate over the mean precipitation. Orange points represent steady state values while blue points represent cases in the oscillatory convection regime. An overbar denotes the time-mean variable.

ocean simulations, the diurnal cycle modulates precipitation to occur in the afternoon to early nighttime hours even as precipitation patterns transitioned to the RO convection regime at mean SSTs around 325 K. However, at high enough surface temperatures, for example, the -100 W m^{-2} slab ocean heat flux with a mean SST of 336 K, the simulation showed a clear episodic deluge regime where precipitation transitioned to occur in the late-night to early morning hours. In the RO regime, lower tropospheric radiative heating (LTRH) increases stability and suppresses convection in the lower troposphere, while longwave cooling in the upper troposphere enhances convective instability. LTRH is strongest during the day and weakest at the end of the night (see Figures 3 and 10). Results from both sets of RCE simulations suggest that convection in the RO regime is triggered when convective instability is weakest, typically during the late-night to early morning hours.

The current 1-km grid under-resolves convection, likely producing overly stiff convection and excessive buildup of convective inhibition, which could bias the outcome. The RCE simulations presented in this work use a small-domain, a 1 km grid spacing that does not fully resolve shallow convection, and the simulations do not consider the effect of large-scale circulations. Using an LES setup is highly idealized and it is unclear how the simulation results would change with a grid that truly resolves shallow convection (with grid spacing of a few hundred meters). However, the simulation setup presented in this work is able to capture the fundamental effect of diurnal variations in the shortwave on the transition to episodic precipitation with both ocean (fixed SST) and swamp-like (slab ocean simulation) boundary conditions.

The slab ocean simulations allow us to capture diurnal variability in the surface temperature but the simulations are not in a statistical equilibrium as the mean SST will continue to increase or decrease over time depending on the initial ocean heat flux value. Additionally, this study solely focused on the transition to episodic precipitation

through changes in the mean SST, but Dagan and Eytan (2024) have shown the transition to RO regimes can also occur due to absorbing aerosols in modern-day SST conditions. The diurnal cycle may also impact RO transitions and extreme precipitation due to absorbing aerosols in current SST conditions.

Adding a diurnal forcing brings the model one step closer to reality and reveals that the diurnal cycle modulates precipitation in the RO regime to occur at dawn and dusk transitions. Even with diurnal forcing, the RCE simulations with both the ocean and swamp-like boundary conditions suggest that the transition to the RO regime emerges at SSTs comparable to those reported in earlier work (Dagan et al., 2023; Seeley & Wordsworth, 2021; Song et al., 2023; Spaulding-Astudillo & Mitchell, 2024). This work highlights that radiative effects are important in the transition to the RO regime for hothouse climates since the transition is based on radiation interacting with an inhibition layer in the lower troposphere. We find that the diurnal cycle affects the LTRH by introducing diurnal variations in convective inhibition strength that affect the behavior of RO convection through the inhibition layer.

In addition to understanding the transition to RO convection from a radiation-driven perspective, we also examined the transition to RO convection using the QE-breakdown hypothesis (Spaulding-Astudillo & Mitchell, 2024), and the Predator-Prey framework (Yang et al., 2024). We evaluated the QE-breakdown framework using both a simulation-based and theoretical calculation. We found the simulations show QE breakdown and the emergence of RO convection in agreement with the simulations and the radiative driven hypothesis. In the simulation-based QE-breakdown framework, RO convection should emerge around 322 K for the fixed SST simulations and near 337 K for the slab ocean simulations. The theoretical prediction of the QE-breakdown hypothesis is that RO convection should emerge around 315 K for both the fixed SST and slab ocean simulations, even across different bulk-plume parameter choices. The QE-breakdown theory predicts an essentially fixed RO transition temperature, indicating that the theory does not capture the difference between the slab ocean and fixed SST simulations, which is the effect of time-varying radiative forcing and surface temperatures. The theoretical prediction under predicts the SST where RO convection emerges relative to the simulation-based prediction for both the fixed SST and slab ocean simulations. This is likely due to the uncertainty in the bulk plume parameter, and simplifying assumptions made in the QE-breakdown theory. The QE-breakdown hypothesis neglects convective inhibition, which could play a larger role than CAPE in regulating the transition to RO convection.

Within the Predator-Prey framework, RO convection emerges at a time-mean CIN of about 8 J kg^{-1} in both the fixed SST and slab ocean simulations, consistent with simulations that show episodic trends within their precipitation timeseries. The transition point of 8 J kg^{-1} is similar to the 9 J kg^{-1} reported by (Yang et al., 2024), with the difference potentially due to diurnal forcing. Future research should investigate the role of inhibition layers in the mechanism and emergence of RO convection regimes. For instance, if near surface inhibition layers can be produced by processes other than radiation (e.g., compositional effects as in Habib & Pierrehumbert, 2024; Leconte et al., 2024), would an RO convection regime still emerge at similar time-mean CIN values?

Although RO convection is typically studied under hothouse conditions, it could also be relevant for exoplanets. Terrestrial planets near the inner edge of the habitable zone, the circumstellar region where liquid water can exist at the surface of a planet, could experience hothouse climates that favor RO behavior (e.g., Wolf & Toon, 2015). So far, no atmosphere has been detected around a terrestrial exoplanet, and convection studies for terrestrial exoplanets remain idealized and based on Earth-like conditions due to the lack of compositional constraints. The most commonly observed group of exoplanets, sub-Neptunes, which have low mean molecular weight atmospheres, could also have RO convection regimes. However, this would require a theoretical exploration of RO convection in low mean molecular weigh atmospheres. While this work uses water vapor as the condensable tracer, exoplanets are known to have a range of exotic atmospheric condensables that impact the net radiative heating rate and could modify both the onset and nature of the RO regime (Seeley & Wordsworth, 2025).

Appendix A: Shallow Versus Deep Slab Ocean Depths

We used slab ocean simulations to capture a large diurnal forcing in the surface temperature. Using a shallow mixed layer in a slab ocean model mimics swamp-like (or even land-like) conditions by capturing large (~10 K) diurnal surface temperature variations. Conversely, using a deep slab ocean model would strongly dampen the diurnal SST variations, making them practically negligible, creating a setup essentially equivalent to the fixed SST case.

To illustrate this effect, we performed an additional slab ocean simulation with a 50 m slab ocean depth and an ocean heat flux of 100 W m^{-2} to balance the observed top-of-atmosphere energy imbalance observed in the fixed SST run at 300 K.

Figure A1 shows SST (K, top row) and precipitation rate (mm day^{-1}, bottom row) for three cases: the 300 K fixed SST simulation (left column), the 0.2 m slab ocean simulation with 100 W m^{-2} ocean heat flux (middle column) and the 50 m slab ocean simulation with 100 W m^{-2} ocean heat flux (right column). The shallow 0.2 m slab ocean depth produces diurnal variations of about 10 K in the surface temperature, whereas the 50 m slab ocean simulation dampens the diurnal variations in the surface temperature to about 0.2 K. In the precipitation rate, the 50 m slab ocean simulation more closely matches the fixed SST simulation rather than the shallow 0.2 m slab ocean case.

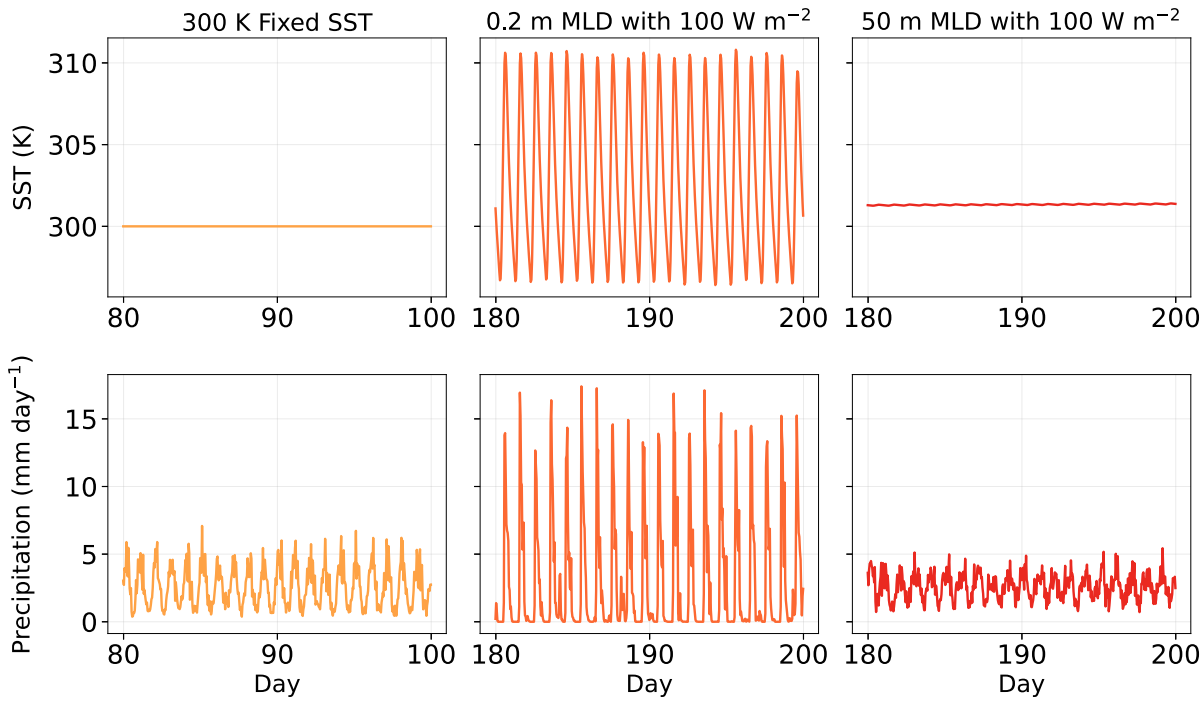

Figure A1. A comparison of the SST (K, top row) and precipitation rate (mm day^{-1}, bottom row) for the 300 K fixed SST simulation (left column), the 0.2 m slab ocean simulation with 100 W m^{-2} ocean heat flux (middle column) and the 50 m slab ocean simulation with 100 W m^{-2} ocean heat flux (right column). The 50 m slab ocean simulation closely resembles the 300 K fixed SST simulation.

The goal of our paper is to understand how diurnal variations impact the transition to an episodic convection regime. The fixed SST simulations represent ocean-like conditions where the diurnal fluctuations in the surface temperature are minimal. Conversely, the slab ocean simulations represent swamp-like conditions where the surface temperature fluctuates with the diurnal cycle. In our slab ocean simulations we use a shallow mixed layer depth the capture large scale diurnal oscillations in the surface temperature.

Conflict of Interest

The authors declare no conflicts of interest relevant to this study.

Data Availability Statement

The convection-resolving model SAM is publicly available at M. Khairoutdinov and Randall (2003) and described by M. F. Khairoutdinov and Randall (2003). The data used in this study is available at Habib et al. (2025).

Acknowledgments
We thank Jake Seeley for discussions in developing this work and Sreelekshmi Thulaseedharan for her help with visualizing the SAM data. G.D. has been supported by the German Research Foundation (DFG) under Grant HO 6588/3–1. We thank the three anonymous reviewers for suggestions that improved the final manuscript.

References

Bechtold, P., Chaboureau, J.-P., Beljaars, A., Betts, A. K., Köhler, M., Miller, M., & Redelsperger, J.-L. (2004). The simulation of the diurnal cycle of convective precipitation over land in a global model. *Quarterly Journal of the Royal Meteorological Society*, *130*(604), 3119–3137. https://doi.org/10.1256/qj.03.103

Charnay, B., Le Hir, G., Fluteau, F., Forget, F., & Catling, D. C. (2017). A warm or a cold early Earth? New insights from a 3-D climate-carbon model. *Earth and Planetary Science Letters*, *474*, 97–109. https://doi.org/10.1016/j.epsl.2017.06.029

Collins, W. D., Rasch, P. J., Boville, B. A., Hack, J. J., McCaa, J. R., Williamson, D. L., et al. (2006). The formulation and atmospheric simulation of the Community Atmosphere Model Version 3 (CAM3). *Journal of Climate*, *19*(11), 2144–2161. https://doi.org/10.1175/JCLI3760.1

Cronin, T. W., Emanuel, K. A., & Molnar, P. (2015). Island precipitation enhancement and the diurnal cycle in radiative-convective equilibrium. *Quarterly Journal of the Royal Meteorological Society*, *141*(689), 1017–1034. https://doi.org/10.1002/qj.2443

Dagan, G. (2022). Equilibrium climate sensitivity increases with aerosol concentration due to changes in precipitation efficiency. *Atmospheric Chemistry and Physics*, *22*(24), 15767–15775. https://doi.org/10.5194/acp-22-15767-2022

Dagan, G., & Eytan, E. (2024). The potential of absorbing aerosols to enhance extreme precipitation. *Geophysical Research Letters*, *51*(10), e2024GL108385. https://doi.org/10.1029/2024GL108385

Dagan, G., Seeley, J. T., & Steiger, N. (2023). Convection and convective-organization in hothouse climates. *Journal of Advances in Modeling Earth Systems*, *15*(11), e2023MS003765. https://doi.org/10.1029/2023MS003765

Dai, A., Lin, X., & Hsu, K.-L. (2007). The frequency, intensity, and diurnal cycle of precipitation in surface and satellite observations over low- and mid-latitudes. *Climate Dynamics*, *29*(7), 727–744. https://doi.org/10.1007/s00382-007-0260-y

Dingley, B., Dagan, G., Stier, P., & Herbert, R. (2023). The impact of a land-sea contrast on convective aggregation in radiative-convective equilibrium. *Journal of Advances in Modeling Earth Systems*, *15*(4), e2022MS003249. https://doi.org/10.1029/2022MS003249

Emanuel, K. A. (1994). *Atmospheric convection*. Oxford University Press.

Emanuel, K. A., & Bister, M. (1996). Moist convective velocity and buoyancy scales.*Journal of the Atmospheric Sciences*, *53*(22), 3276–3285. https://doi.org/10.1175/1520-0469(1996)053<3276:MCVABS>2.0.CO;2

Habib, N., Dagan, G., & Steiger, N. (2025). *Assessing the influence of diurnal variability on the transition from steady State to episodic convection in hothouse climates*. Zenodo. Retrieved from https://zenodo.org/records/14755292

Habib, N., & Pierrehumbert, R. T. (2024). Modeling noncondensing compositional convection for applications to Super-Earth and Sub-Neptune atmospheres. *The Astrophysical Journal*, *961*(1), 35. https://doi.org/10.3847/1538-4357/ad04e2

Habib, N., & Pierrehumbert, R. T. (2025). 3D modeling of moist convective inhibition in idealized Sub-Neptune atmospheres. *The Astrophysical Journal*, *995*(1), 41. https://doi.org/10.3847/1538-4357/ae147c

Haerter, J. O., Meyer, B., & Nissen, S. B. (2020). Diurnal self-aggregation. *npj Climate and Atmospheric Science*, *3*(1), 1–11. https://doi.org/10.1038/s41612-020-00132-z

Jeevanjee, N., & Romps, D. M. (2018). Mean precipitation change from a deepening troposphere. *Proceedings of the National Academy of Sciences*, *115*(45), 11465–11470. https://doi.org/10.1073/pnas.1720683115

Jensen, G. G., Fiévet, R., & Haerter, J. O. (2022). The diurnal path to persistent convective self-aggregation. *Journal of Advances in Modeling Earth Systems*, *14*(5), e2021MS002923. https://doi.org/10.1029/2021MS002923

Khairoutdinov, M., & Randall, D. A. (2003). System for atmospheric modeling. Retrieved from http://rossby.msrc.sunysb.edu/SAM.html

Khairoutdinov, M. F., & Randall, D. A. (2003). Cloud resolving modeling of the ARM summer 1997 IOP: Model formulation, results, uncertainties, and sensitivities. *Journal of the Atmospheric Sciences*, *60*(4), 607–625. https://doi.org/10.1175/1520-0469(2003)060<0607:CRMOTA>2.0.CO;2

Leconte, J., Spiga, A., Clément, N., Guerlet, S., Selsis, F., Milcareck, G., et al. (2024). A 3D picture of moist-convection inhibition in hydrogen-rich atmospheres: Implications for K2-18 b. *Atronomy & Astrophysics*, *686*, A131. https://doi.org/10.1051/0004-6361/202348928

Liu, C., & Moncrieff, M. W. (1998). A numerical Study of the diurnal cycle of tropical Oceanic convection. *Journal of the Atmospheric Sciences*, *55*(13), 2329–2344. https://doi.org/10.1175/1520-0469(1998)055<2329:ANSOTD>2.0.CO;2

Nicholls, M. E. (2015). An investigation of how radiation may cause accelerated rates of tropical cyclogenesis and diurnal cycles of convective activity. *Atmospheric Chemistry and Physics*, *15*(15), 9003–9029. https://doi.org/10.5194/acp-15-9003-2015

O'Gorman, P. A., Allan, R. P., Byrne, M. P., & Previdi, M. (2012). Energetic constraints on precipitation under climate change. *Surveys in Geophysics*, *33*(3), 585–608. https://doi.org/10.1007/s10712-011-9159-6

Pierrehumbert, R. T. (2002). The hydrologic cycle in deep-time climate problems. *Nature*, *419*(6903), 191–198. https://doi.org/10.1038/nature01088

Pierrehumbert, R. T. (2010). *Principles of planetary climate*. Cambridge University Press.

Popp, M., Schmidt, H., & Marotzke, J. (2016). Transition to a moist greenhouse with CO2 and solar forcing. *Nature Communications*, *7*(1), 10627. (Publisher: Nature Publishing Group UK London). https://doi.org/10.1038/ncomms10627

Romps, D. M. (2016). Clausius–Clapeyron scaling of CAPE from analytical solutions to RCE. *Journal of the Atmospheric Sciences*, *73*(9), 3719–3737. https://doi.org/10.1175/JAS-D-15-0327.1

Romps, D. M. (2020). Climate sensitivity and the direct effect of carbon dioxide in a limited-area cloud-resolving model. *Journal of Climate*, *33*(9), 3413–3429. https://doi.org/10.1175/JCLI-D-19-0682.1

Ruppert, J. H., & Hohenegger, C. (2018). Diurnal circulation adjustment and organized deep convection. *Journal of Climate*, *31*(12), 4899–4916. https://doi.org/10.1175/JCLI-D-17-0693.1

Sato, T., Miura, H., Satoh, M., Takayabu, Y. N., & Wang, Y. (2009). Diurnal cycle of precipitation in the tropics simulated in a global cloud-resolving model. *Journal of Climate*, *22*(18), 4809–4826. https://doi.org/10.1175/2009JCLI2890.1

Seeley, J. T., & Romps, D. M. (2015). Why does tropical Convective Available Potential Energy (CAPE) increase with warming? *Geophysical Research Letters*, *42*(23), 10429–10437. https://doi.org/10.1002/2015GL066199

Seeley, J. T., & Wordsworth, R. D. (2021). Episodic deluges in simulated hothouse climates. *Nature*, *599*(7883), 74–79. (Publisher: Nature Publishing Group UK London). https://doi.org/10.1038/s41586-021-03919-z

Seeley, J. T., & Wordsworth, R. D. (2025). Resolved convection in hydrogen-rich atmospheres. *The Planetary Science Journal*, *6*(1), 6. https://doi.org/10.3847/PSJ/ad9b1a

Singh, M. S., & O'Gorman, P. A. (2013). Influence of entrainment on the thermal stratification in simulations of radiative-convective equilibrium. *Geophysical Research Letters*, *40*(16), 4398–4403. https://doi.org/10.1002/grl.50796

Sleep, N. H. (2010). The Hadean-Archaean environment. *Cold Spring Harbor Perspectives in Biology*, *2*(6), a002527. https://doi.org/10.1101/cshperspect.a002527

Song, X., Abbot, D. S., & Yang, J. (2023). Critical role of vertical radiative cooling contrast in triggering episodic deluges in small-domain hothouse climates. *arXiv*. https://doi.org/10.48550/arXiv.2307.01219

Spaulding-Astudillo, F. E., & Mitchell, J. L. (2024). A simple model for the emergence of relaxation-oscillator convection. *Journal of Advances in Modeling Earth Systems*, *16*(11), e2024MS004439. https://doi.org/10.1029/2024MS004439

Wing, A. A., Reed, K. A., Satoh, M., Stevens, B., Bony, S., & Ohno, T. (2018). Radiative–convective equilibrium model intercomparison project. *Geoscientific Model Development*, *11*(2), 793–813. https://doi.org/10.5194/gmd-11-793-2018

Wolf, E. T., & Toon, O. B. (2015). The evolution of habitable climates under the brightening Sun. *Journal of Geophysical Research: Atmospheres*, *120*(12), 5775–5794. https://doi.org/10.1002/2015JD023302

Yang, D., Abbot, D. S., & Seidel, S. (2024). Predator and prey: A minimum recipe for the transition from steady to oscillating precipitation in hothouse climates. *arXiv*. https://doi.org/10.48550/arXiv.2408.11350